Numerical Computations of Wind Turbine Wakes

by

Stefan S. A. Ivanell

April 2005
Technical Reports from
KTH Mechanics
Royal Institute of Technology
SE-100 44 Stockholm, Sweden

Front cover illustration shows a close up of the tip vortex, here illustrated by inserting smoke into the flow field. The turbine is positioned, to the right, outside the illustration. [Montgomerie, Dahlberg]

Typsatt i $\mathcal{AMS}$-LaTeX.

Akademisk avhandling som med tillstånd av Kungliga Tekniska högskolan i Stockholm framlägges till offentlig granskning för avläggande av teknologie licentiatexamen fredagen den 20:e maj 2005 kl 10:15 i sal E36, KTH, Stockholm.

Universitetsservice US AB, Stockholm 2005

.

To Ida and Anton

S. Ivanell 2005, **Numerical Computations of Wind Turbine Wakes**

KTH Mechanics, Royal Institute of Technology
SE-100 44 Stockholm, Sweden

Abstract

Numerical simulations using CFD methods are performed for wind turbine applications. The aim of the project is to get a better understanding of the wake behaviour, which is needed since today's industrial design codes for wind power applications are based on the BEM (Blade Element Momentum) method. This method has been extended with a number of empirical corrections not based on physical flow features. The importance of accurate design models does also increase as the turbines become larger. Therefore, the research is today shifting toward a more fundamental approach, aiming at understanding basic aerodynamic mechanisms. The result from the CFD simulation is evaluated and special interest is given to the circulation and the position of vortices. From these evaluations, it will hopefully be possible to improve the engineering methods and base them, to a greater extent, on physical features instead of empirical corrections.

The simulations are performed using the program "EllipSys3D" developed at DTU (The Technical University of Denmark). The Actuator Line Method is used, where the blade is represented by a line instead of a large number of panels. The forces on that line are introduced by using tabulated aerodynamic coefficients. In this way, the computer resource is used more efficiently since the number of node points locally around the blade is decreased, and they can instead be concentrated in the wake behind the blades.

An evaluation method to extract values of the circulation from the wake flow field is developed.

The result shows agreement with classical theorems from Helmholtz, from which it follows that the wake tip vortex has the same circulation as the maximum value of the bound circulation on the blade.

Descriptors: Wind Energy, Wind Turbine, Wake, Circulation, Vortex, CFD, EllipSys3D, Actuator line.

Preface

This licentiate thesis is a result of cooperation between Gotland University, Sweden, The Royal Institute of Technology, Stockholm, Sweden, and The Swedish Defence Research Agency.

I would like to thank the Swedish Energy Agency for financing the major part of this project. I would also like to thank Gotland University and The Royal Institute of Technology for their generous economic support during the last part of this project.

I wish to express my sincere thanks to my adviser, Professor Dan Henningson, at the Royal Institute of Technology, for his encouraging support.

Special thanks to Björn Montgomerie, at The Swedish Defence Research Agency, for his enthusiastic support and many interesting discussions.

Great thanks to professor Jens Sørensen and his colleagues, Robert Mikkelsen and Jess Michaelsen among others, at The Technical University of Denmark, Copenhagen. We had many interesting discussions during my visits to DTU. You always made me feel welcome, thanks for that. Special thanks to Jess who gave me access to run my computations at the new Linux cluster and for sharing the EllipSys3D code.

Special thanks to Robert, without his support of the EllipSys3D and the actuator line method, this project would not have been completed during this project time. Sincere thanks for all hours you spent with me during late evenings at DTU and also for the nice company during evenings in Copenhagen.

Of course I also would like to thank my Ph.D.-student colleagues at the Mechanical department at the Royal Institute of Technology for all interesting discussions during different courses and projects.

At last, I would like to express my sincere thanks to my colleagues at Gotland University, who provided me with a very nice and friendly environment and also for a great understanding when I concentrated my time on the research in this project, even when the workload in other projects has been high.

Visby, April 15 2005

Stefan S. A. Ivanell

Contents

Nomenclature

Roman letters

a	Axial induction factor	[-]
a'	The local speed ratio	[-]
b	Blade index	[-]
A, A_2	Turbine area	$[m^2]$
B	Number of blades	[-]
c	Chord	[m]
C_d	Drag coefficient	[-]
C_l	Lift coefficient	[-]
c_m	Mean chord	[m]
C_p	Power coefficient	[-]
C_T	Thrust coefficient	[-]
C_{T1}	Empirical thrust coefficient	[-]
d	Prantl disc distance	[m]
dF_D	Section drag force	[N]
dF_L	Section lift force	[N]
dF_N	Section thrust force	[N]
dF_T	Section torque force	[N]
$\mathbf{D}$	Drag force	[N/m]
$\mathbf{e}_L$	Lift unit vector	[-]
$\mathbf{e}_D$	Drag unit vector	[-]
$\mathbf{f}$	Areal loading	$[N/m^2]$
$\mathbf{f}'$	Volume force	$[N/m^3]$
F	Prantl's tip loss factor	[-]
$\mathbf{F}$	Loading	[N/m]
H_{after}	Total head behind ACD	$[N/m^2]$
H_{before}	Total head in front of ACD	$[N/m^2]$
$\mathbf{L}$	Lift force	[N/m]
$\dot{m}$	Mass flow rate	[kg/s]
N	Number of blade sections	[-]
p_∞	Undisturbed pressure	$[N/m^2]$
p_2	Pressure close before turbine	$[N/m^2]$
p_3	Pressure close behind turbine	$[N/m^2]$
p_4	Pressure far behind turbine	$[N/m^2]$
P	Rotor power	[W]
Q	Torque	[Nm]
r	Radial position	[m]
R	Turbine radius	[m]
R_w	Radial position in wake	[m]
S	Integration path	[m]

T	Thrust force	[N]
U_∞	Undisturbed wind speed	[m/s]
U_{rel}	Relative wind velocity	[m/s]
U_2	Wind velocity close before turbine	[m/s]
U_3	Wind velocity close behind turbine	[m/s]
U_4	Wind velocity far behind turbine	[m/s]
W	Induced velocity	[m/s]

Greek letters

α	Angle of attack	[-]
γ	Angle behind ACL	[°]
Γ	Circulation	$[m^2/s]$
ϵ	Gaussian smearing function	[-]
ζ	Vorticity	[1/s]
θ_p	Section pitch angle	[°]
$\theta_{p,0}$	Blade pitch angle	[°]
θ_T	Twist angle	[°]
λ	Tip speed ratio	[-]
λ_r	Axial induction factor	[-]
μ	Non-dimensional radial position	[-]
ν	Kinematic viscosity	$[m^2/s]$
ρ	Density	$[kg/m^3]$
σ	Turbine solidity	[-]
σ'	Local solidity	[-]
ω	Angular velocity	[rad/s]
Ω	Angular velocity	[rad/s]
ϕ	Relative wind angle	[°]
ϕ_{tip}	Relative wind angle at blade tip	[°]
Ψ	Stream function	$[m^3/s]$

Acronyms

ACD	Actuator Disc
ACL	Actuator Line
BE	Blade Element
BEM	Blade Element Momentum
CDS	Central difference Schemes)
DES	Detached-Eddy Simulation
CFD	Computational Fluid Dynamics
DNS	Direct Numerical Simulation
DTU	The Technical University of Denmark

FOI	The Swedish Defence Research Agency
HGO	Gotland University
KTH	The Royal Institute of Technology
LES	Large Eddy Simulation
MEXICO	Model Rotor Experiments under Controlled Conditions
MPI	Message Passage Interface
NREL	National Renewable Energy Laboratory
QUICK	Quadratic Upstream Interpolation for Convection Kinematics
RANS	Reynolds Average Navier-Stokes

CHAPTER 1

Introduction

1.1. Some historical remarks

Today wind turbines are the largest rotating machines on earth. They are also the oldest device for exploring the energy of the wind on land. In fact, the only older device for exploring wind energy in general is the sailing ship. The first documented use of wind energy on land was made in 947, [Wizelius]. It was a windmill in Persia close to the border of Afghanistan. However, it is said that some type of windmill was used as early as 3000 years ago in China and Japan, [Wizelius]. Wind turbines have without any doubt been very important for the evolution of modern society. The turbine will also turn out to be very important in the future.

1.2. The aim of the project

The knowledge about the wind power technology has increased over the years. Lanchester [Lanchester 1915] and Betz [Betz 1920] were the first to predict the maximum power output of an ideal wind turbine. The major break-through was achieved by Glauert who formulated the Blade Element Momentum (BEM) method in 1935 [Glauert 1935], which will be discussed in section 2.2.6.

Today's design codes are still based on the Blade Element Momentum method (BEM). It has however been extended, to allow for dynamic events, with patch work and add hoc engineering methods, sometimes of doubtful quality.

Therefore, the aerodynamic research is today shifting toward a more fundamental approach since the basic aerodynamic mechanisms are not fully understood and the importance of accurate design models increases when the turbines are becoming larger.

Recently, complete Naiver Stokes calculations have been performed and today supercomputers opens new possibilities.

The aim of this project is to evaluate existing aerodynamic simulation methods to hopefully be able to run simulations that give satisfactory results making it possible to evaluate the flow field behind the turbine, i.e. the wake. From these simulations, the physical behaviour of the wake will be studied. Particular attention will be given to the circulation close behind the blades.

1.3. The AEROBIG project

This project is a part of the AEROBIG project which involves five persons; Project manager Björn Montgomerie, Professor Dan Henningson, Hans Ganander, Ingemar Carlén and Stefan Ivanell. The aim of AEROBIG is to develop design codes that are more accurate than existing codes. Physical features rather than empirical corrections will be utilized to a greater extent. Hans Ganander and Ingemar Carlén, Teknikgruppen, deals with the solid mechanical aspects of the project, Björn Montgomerie, FOI, deal with the designing of

the aerodynamic engineering methods. The task of this part of the project is then to evaluate the circulation in the wake with the best tool available to give a better understanding of the physics close behind the blades.

Results from the AEROBIG project, other than this report, are found in references [Montgomerie 2004a], [Montgomerie 2004b], [Åhlund], [Carlén 2005a], [Carlén 2005b] and [Ganander].

1.4. Introduction to the functioning of modern wind turbines

In this section the basic features of a modern wind turbine is described. The aim here is to give a brief explanation of how a modern turbine works, not only in an aerodynamic sense, but also in general. This section is mostly written as a brief background for readers who are familiar with aerodynamics but who lack knowledge about wind turbines in general.

Wind turbines transform the energy in the wind to useful energy. Older turbines, like a windmill or a pump station transformed the energy into mechanical energy. Today's modern turbines transform the energy to electric power. This transformation consists of many complicated steps. Today's turbines are advanced machines that use the latest available technology in many different fields, for example aerodynamics, mechanics, machine technology, electro technology, control systems, solid mechanics etc. If one also considers that they are the largest existing rotating machines, and that increasing size invites more complicated dynamics, one can understand that it is a challenge for engineers to design one.

When the wind is caught by the blades of the turbine, the blades are affected by a force which makes them rotate for the same reason that makes an airplane flying. I.e. the aerodynamic lifting force is used to drive the rotor, thus generating the shaft torque, which is then transferred into the generator. Some turbines have a gearbox, some do not, depending on the type of generator.

The three most common setups are described here;

- Type 1: A classical turbine with gearbox, "The Danish model". The shaft from the turbine is connected to a gearbox, which by a number of steps, typically 3, increases the rotational velocity of the outgoing axle, which then is connected to the generator. The generator itself is then connected to the electrical grid. There is off course a number of different ways to construct the generator and the connection to the electrical grid but that has been left out in this report.

- Type 2: A turbine without gearbox. Here the axle is connected directly to the generator. Because of the low rotational velocity, same as for the turbine, this results in a much larger multi-pole generator. The need to encase this large generator leads to a larger nacelle. In fact, the multi-pole generator seems to outweigh the combination of gear box

and standard 4-pole generator.

- Type 3: Hybrid. This third type is a combination of the previous two. It does have a gearbox as type 1 but with fewer steps, typically one. This means a smaller gearbox but since the angular velocity is not increased as much as for type 1, the generator is in this case larger than for type 1, but not as large as for type 3.

Almost all modern turbines have variable angular velocity. This means that the turbine is resilient to the variable wind. A sudden increase in wind speed can be absorbed by an increase in angular velocity instead of producing a large torque on the power train. The variable angular velocity therefore decreases the fatigue loading on the turbine.

The turbine must yaw into the wind at all times. On top of the nacelle there is an anemometer and a wind vane which measures wind speed and the direction of the wind. When the wind direction changes the nacelle is turned by, typically 2 or 4, electric motors. These motors are positioned inside a cog ring at the top of the tower.

A turbine starts when the mean velocity in the wind is about 3-5 m/s. The turbine then transforms as much energy as possible until the rated power to the generator is reached. Then the excess power must be avoided somehow. There are typically three ways to do that.

- Stall control
  When stall control is used, the blades are aerodynamically designed to lose lift force at a certain angle of attack. The turbine is therefore constructed in a way that makes sure that when the limit on the generator is reached, then the angle of attack where the stall effect starts is reached too. When the wind then increases even more, then the lift force of the blades also decreases because of increasing stall. Stall is achieved by maintaining constant rotor RPM while the increasing wind speed causes increasing of the angle of attack radial distribution.

- Pitch control
  When pitch control is used, the blades are turned (pitched) to loose lift force.

- Active stall
  Active stall control triggers stall intentionally. Once in stall only very small pitch excursions are required to give shorter response times than these of pitch-to-avoid stall control.

Irrespective of control system, the turbine is stopped at a critical wind speed, typically 25 m/s, for safety reasons.

All turbines have two independent brake systems. The brake systems are used for emergency stops and when maintenance is needed. The turbines are equippt with an aerodynamic and a mechanical brake. The design of the aerodynamic brake depends on the control system, a stall controlled turbine has pitchable blade tips. A pitch controlled turbine turns the whole blades.

The mechanical brake system consists of a disk brake. For turbines with gearbox the brake is positioned on the axle, with highest rotational velocity, out from the gearbox. In that way the brake efficiency is increased, the drawbacks is that if the gearbox for some reason breaks, the mechanical brake is out of function. For turbines without gearbox the brake is positioned on the main axle.

When a turbine is stopped in a controlled way, the aerodynamic brake reduces the angular velocity to a great extent, before the mechanical brake is applied. If an emergency occurs both brake systems are activated at the same time.

Both brake systems are "active", i.e. a force is acting to deactivate them. Therefore, if something goes wrong, for example a power failure, the brakes are applied automatically without any applied force or control system.

The largest turbine built today has a generator of about 5 MW. A turbine of that size will in a generally good wind site produce about 10 GWh of electrical energy per year. This is sufficient to provide the energy for 500 electrically heated normal size one-family houses in Sweden, or for 2000 houses with other heating system, or for 5000 flats.

CHAPTER 2

Classical Aerodynamic Models

This chapter will treat the basic theory for different classical aerodynamic models. The following models will be treated:

- One-Dimensional Momentum Theory
- Ideal Horizontal Axis Wind Turbine with Wake Rotation
- Blade Element Method (BE)
- Blade Element Momentum Method (BEM)

For readers familiar with wind energy aerodynamics, this chapter could be omitted without causing any misunderstanding in the following chapters. The theory in this chapter has been summarized from references [Glauert 1935], [Freris], [Burton et al], [Wilson 1998] and [Manwell et al].

2.1. Basic definitions

Tip speed ratio

The tip speed ratio is a very important parameter. It expresses the ratio between the tip speed and the undisturbed wind speed.

$$\lambda = \frac{\Omega R}{U_\infty} \tag{2.1}$$

where Ω is the angular velocity, R the radius of the blades and U_∞ the undisturbed wind speed. The tip speed ratio dictates the operating condition of a turbine and it affects a number of flow parameters that will be discussed later.

Turbine solidity

The turbine solidity is defined as the ratio between the blade area to the area of the disk. It is the primary non-dimensional factor which describes the geometry of the turbine.

$$\sigma = \frac{Total\ blade\ area}{Disc\ area} \tag{2.2}$$

Local turbine solidity

The local turbine solidity is defined in the same manner as the turbine solidity, only now defined locally at certain radius.

$$\sigma' = \frac{Bc(r)}{2\pi r} \tag{2.3}$$

where B is the number of blades and c the chord of the blades.

Power coefficient

The power coefficient corresponds to the relation between the rotor power and the power in the wind:

$$C_p \equiv \frac{P}{\frac{1}{2}A\rho U_\infty^3} \tag{2.4}$$

where ρ is the air density, A the turbine area, U_∞ the free stream velocity.

2.2. Aerodynamic models

2.2.1. *One-dimensional momentum theory and the Betz limit*

This model, originated by Rankine [1895] but generally attributed to Betz [1926], is based on linear momentum theory. Originally it was developed to predict performance of ship propellers. The model uses a tube-like control volume. A uniform "actuator disk", which creates a discontinuity of the pressure, represents the turbine.

This model uses a number of assumptions that gives a more simple model. The model gives results, which to a first approximation are in good agreement with measurements, and these results are often used as a reference.

The following assumptions are used:

- The flow passing trough the disk can be separated from the rest of the flow by a well defined stream tube.
- Entirely axial flow
- Homogeneous, incompressible, steady flow
- No friction drag
- An infinite number of blades, i.e. the velocity is constant over the disk area and the thrust uniform on the disk area
- Rotation imposed on the flow as it passes through the disk is neglected, i.e. a non rotating wake.
- The static pressure far upstream and far downstream of the rotor is equal to the undisturbed ambient static pressure, more comments about it in section 2.2.3.

For steady state flow $(\rho AU)_\infty = (\rho AU)_4 = \dot{m}$ where $\dot{m}$ is the mass flow rate and the index 4 notes the position according to figure 2.1. The thrust force is therefore equal to the mass flow multiplied with the change in velocity.

$$T = \dot{m}(U_\infty - U_4) \tag{2.5}$$

Applying requirements for continuity, momentum balance, and energy balance to the flow, the thrust and power can be determined if the assumptions above are fulfilled.

Firstly, from the momentum theorem, the thrust is:

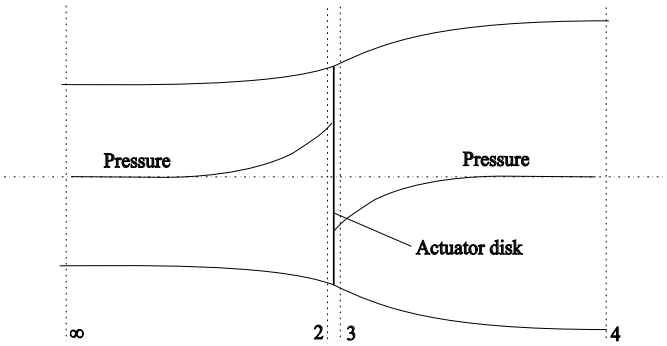

FIGURE 2.1. The actuator disc concept.

$$T = U_\infty(\rho AU)_\infty - U_4(\rho AU)_4 \tag{2.6}$$

where ρ is the air density, A the cross section area, U_∞ the free stream velocity and U_2, U_3, U_4 the velocities at different locations according to figure 2.1.

Secondly, from the consideration of the pressure drop caused by the actuator disk, which represents the turbine, the thrust can also be derived by using the Bernoulli function separately on each side of the turbine.

In the stream tube upstream of the disk:

$$p_\infty + \frac{1}{2}\rho U_\infty^2 = p_2 + \frac{1}{2}\rho U_2^2 \tag{2.7}$$

In the stream tube downstream of the disk:

$$p_3 + \frac{1}{2}\rho U_3^2 = p_4 + \frac{1}{2}\rho U_4^2 \tag{2.8}$$

Since, two of the assumptions for this model are that $p_\infty = p_4$ and that the velocity across the disk remains the same ($U_2 = U_3$), the thrust can also be expressed as:

$$T = A(p_2 - p_3) \tag{2.9}$$

If one solves equation (2.7) and (2.8) for $(p_2 - p_3)$ and substitutes that into (2.9) one obtains:

$$T = \frac{1}{2}\rho A_2(U_\infty^2 - U_4^2) \tag{2.10}$$

Combining (2.5) and (2.10) gives:

$$\dot{m}(U_\infty - U_4) = \frac{1}{2}\rho A_2(U_\infty^2 - U_4^2) \tag{2.11}$$

Recognizing that $\dot{m} = \rho A_2 U_2$ or $\dot{m} = \rho A_3 U_3$ (lets use index 2 for the disk from now on), one gets the result generally known as Froude's theorem.

$$U_2 = \frac{U_\infty + U_4}{2} \tag{2.12}$$

The interpretation of this expression is that the velocity at the disk is the average of the free stream and far wake velocities, so the total velocity change from free-stream to far-wake is twice the change from free stream to the disk.

Now introducing the axial induction factor which is a measure of the turbine influence to the wind and is defined as:

$$a = \frac{U_\infty - U_2}{U_\infty} \tag{2.13}$$

which gives:

$$U_2 = U_\infty(1 - a) \tag{2.14}$$

$$U_4 = U_\infty(1 - 2a) \tag{2.15}$$

The theory is applicable when a is between 0 and $0,5$ since the velocity has slowed to zero behind the rotor for higher values, which is not physically possible. In fact, the theory breaks down about a = 0.35.

From the first law of thermodynamics assuming isothermal flow and ambient pressure in the far wake, power is equal to the thrust times the velocity at the disk.

$$P = \frac{1}{2}\rho A_2(U_\infty^2 - U_4^2)U_2 = \frac{1}{2}\rho A_2(U_\infty - U_4)(U_\infty + U_4)U_2 \tag{2.16}$$

substituting equation (2.14) and (2.15) gives:

$$P = \frac{1}{2}\rho A_2 U_\infty^3 4a(1 - a)^2 \tag{2.17}$$

Using equation (2.4) gives the power coefficient for the actuator disk:

$$C_p = \frac{P}{\frac{1}{2}\rho U_\infty^3 A_2} = 4a(1 - a)^2 \tag{2.18}$$

The power coefficient corresponds to the rotor power divided by the power in the wind. If we put $\frac{dC_p}{da} = 0$ we will get a for maximum C_p.

$$\frac{dC_p}{da} = 4(1 - a)^2 - 8a(1 - a) = 4(1 - 4a + 3a^2) = 0 \tag{2.19}$$

which gives a maximum C_p when $a = \frac{1}{3}$

$$C_{p_{max}} = \frac{16}{27} \tag{2.20}$$

The results shows that with the given assumptions, the maximum theoretical power production is 16/27 of the power in a circular stream-tube with a constant cross section area equal to the disk area. If the free stream velocity is U_∞, then the velocity at the disk is $\frac{2}{3}U_\infty$ and at the end of the stream tube it is $\frac{1}{3}U_\infty$. Therefore, because of continuity, the tube has a cross section area that is $2/3$ of the disk area upstream of the disk and twice the disk area downstream. $C_{p_{max}}$ is generally known as the Betz limit.

The thrust force can be expressed in a similar manner as the power. The non-dimensional thrust coefficient corresponds to the thrust force divided by the dynamic force and can be expressed as:

$$C_T = \frac{T}{\frac{1}{2}\rho U_\infty^2 A_2} \tag{2.21}$$

Combining equation (2.10) and (2.15) gives:

$$T = \frac{1}{2}\rho A_2 U_\infty^2 \{4a(1-a)\} \tag{2.22}$$

which gives:

$$C_T = \frac{\frac{1}{2}\rho A_2 U_\infty^2 \{4a(1-a)\}}{\frac{1}{2}\rho U_\infty^2 A_2} = 4a(1-a) \tag{2.23}$$

In figure 2.2 it is possible to see that the highest power is reached when $a = 1/3$. There are, however, effects that decrease the maximum power that have not been considered here, for example, wake rotation, finite number of blades and profile drag.

2.2.2. *Ideal horizontal axis wind turbine with wake rotation*

In the previous model the flow behind the rotor was assumed to be non-rotating. In reality, the flow behind the rotor rotates in the opposite direction to the rotor, as a reaction to the torque exerted by the flow on the rotor.

The energy extraction by the rotor will be less if one considers the generation of rotational kinetic energy than if one neglects it as in the previous model.

There is a close relation between the generated kinetic energy in the wind turbine wake and the torque. The kinetic energy in the wake will be higher if the torque is higher. Therefore, a machine with low rotational speed and

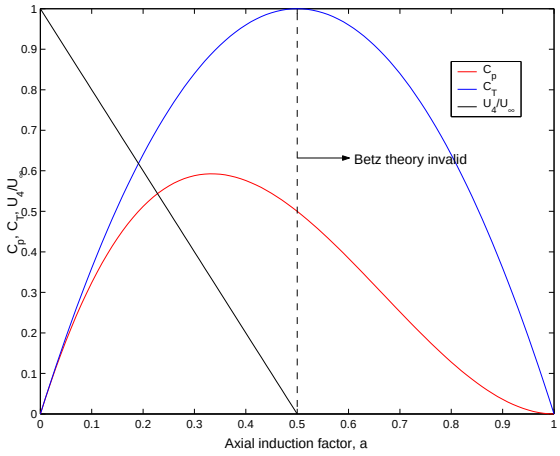

FIGURE 2.2. Momentum Theory. The theory is, however, not valid for large values of a, more comments about it later.

high torque will have higher energy losses than a machine with high rotational speed and low torque.

In this model, the control volume is divided into partial stream tubes with a radial differential extent, see figure 2.3. The energy equation can now be applied in sections before and after the blades to derive an expression for pressure difference across the blades, [Glauert 1935].

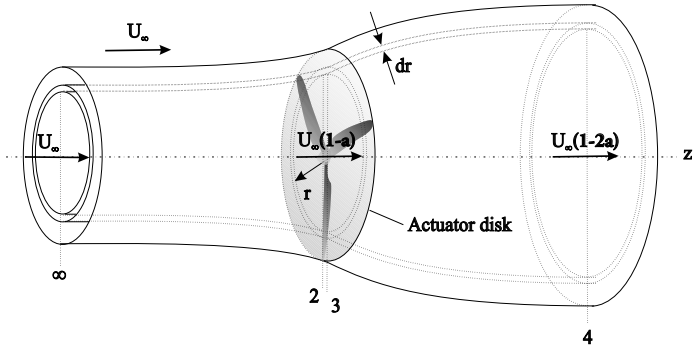

FIGURE 2.3. Control volume that moves with the angular velocity of the blades.

The following assumptions are made:

- The partial stream tubes are assumed to slide without friction, or other interference, on each other.

- The pressure in the far wake is equal to the pressure in the free stream [Wilson et al., 1976]. Further comments in section 2.2.3.
- The pressure, wake rotation and induction factors are all assumed to be a function of radius.

The angular velocity of the air relative to the blades increases from Ω to $\Omega + \omega$ through the disk. The axial velocity on the other hand does not change as rapidly through the disk.

Bernoulli's equation can be applied on each side of the turbine disc. Let u and v be respectively the axial and radial components of the fluid velocity.

$$H_{before} = p_\infty + \frac{1}{2}\rho U_\infty^2 = p_2 + \frac{1}{2}\rho(u_2^2 + v_2^2) \tag{2.24}$$

$$H_{after} = p_2 - p' + \frac{1}{2}\rho(u_3^2 + v_3^2 + \omega_3^2 r_3^2) = p_4 + \frac{1}{2}\rho(u_4^2 + \omega_4^2) \tag{2.25}$$

where H_{before} and H_{after} is the total head before and after the turbine disc and p' the pressure difference across the disc.

$$H_{after} - H_{before} = -p' + \frac{1}{2}\rho\omega_3^2 r_3^2 \tag{2.26}$$

which shows that the decrease of total head on passing thought the turbine disc exceeds the trust per unit area p' by a small term representing the kinetic energy of the rotational motion imparted to the fluid by the torque of the turbine. The expression for the total pressure head also gives:

$$p_\infty - p_4 = \frac{1}{2}\rho(u_4^2 - U_\infty^2) + \frac{1}{2}\rho\omega_4^2 r_4^2 - (H_{after} - H_{before}) \tag{2.27}$$

$$p_\infty - p_4 = \frac{1}{2}\rho(u_4^2 - U_\infty^2) + \frac{1}{2}\rho(\omega_4^2 r_4^2 - \omega_3^2 r_3^2) - p' \tag{2.28}$$

Applying Bernoulli's equation to the flow relative to the turbine blades which are rotating with the angular velocity Ω, the relative angular velocity increases from Ω to $(\Omega + \omega)$ and hence the decrease of pressure is:

$$p' = -\rho(\Omega + \frac{1}{2}\omega)\omega r^2 \tag{2.29}$$

The resulting thrust on an annular element, dT, is:

$$dT = (p_2 - p_3)dA = \left\{\rho(\Omega + \frac{1}{2}\omega)\omega r^2\right\} 2\pi r dr \tag{2.30}$$

We now introduce the angular induction factor which is defined in the same manner as the axial induction factor, only now for the angular component.

$$a' = \frac{\omega}{2\Omega} \tag{2.31}$$

The induced velocity at the rotor now consists of two components, i.e. the axial and angular components. The axial component is still aU_∞, the angular component can be expressed as $r\Omega a'$.

The expression for thrust now becomes:

$$dT = 4a'(1+a')\frac{1}{2}\rho\Omega^2 r^2 \pi r dr \tag{2.32}$$

The thrust force was in the linear momentum model determined to be $\frac{1}{2}\rho A U_\infty^2\{4a(1-a)\}$ which gives dT to:

$$dT = 4a(1-a)\frac{1}{2}\rho U_\infty^2 2\pi r dr \tag{2.33}$$

Now combining the two expressions for thrust gives:

$$\frac{a(1-a)}{a'(1+a')} = \frac{\Omega^2 r^2}{U_\infty^2} \tag{2.34}$$

The tip speed ratio, λ, is defined as the ratio of the blade tip speed to the the free stream wind speed.

$$\lambda = \frac{\Omega R}{U_\infty} \tag{2.35}$$

In the same manner, the local speed ratio is defined as the ratio of the blade speed, at an intermediate radius, and the free stream wind speed.

$$\lambda_r = \frac{\Omega r}{U_\infty} = \frac{\lambda r}{R} \tag{2.36}$$

Equation (2.34) now becomes:

$$\frac{\Omega^2 r^2}{U_\infty^2} = \lambda_r^2 \tag{2.37}$$

Considering the conservation of angular momentum, the torque exerted on the rotor, Q, must equal the change in angular momentum of the wake. The torque on a annular area element is:

$$dQ = d\dot{m}(\omega r)(r) = (\rho U_2 2\pi r dr)(\omega r)(r) \tag{2.38}$$

Since $U_2 = U_\infty(1-a)$ and $a' = \omega/2\Omega$, this expression reduces to:

$$dQ = 4a'(1-a)\frac{1}{2}\rho U_\infty \Omega r^2 2\pi r dr \tag{2.39}$$

The power generated at each element, dP, is given by:

$$dP = \Omega dQ \tag{2.40}$$

Using equation (2.40), (2.36) and (2.39) gives dP as follows:

$$dP = \frac{1}{2}\rho A U_\infty^3 \{\frac{8}{\lambda^2} a'(1-a)\lambda_r^3 d\lambda_r\} \tag{2.41}$$

The contribution to the power from each annular ring is dependent of the axial and angular induction factors and the tip speed ratio, i.e. the direction and magnitude of the airflow at the rotor plane is determined by the induction factors.

Each annular ring gives the following contribution to the power coefficient:

$$dC_p = \frac{dP}{\frac{1}{2}\rho A U_\infty^3} \tag{2.42}$$

C_p now becomes:

$$C_p = \frac{8}{\lambda^2}\int_0^\lambda a'(1-a)\lambda_r^3 d\lambda_r \tag{2.43}$$

To integrate this expression one needs to relate a, a' and λ_r. From equation (2.34) and (2.37) one gets:

$$a' = -\frac{1}{2} \pm \sqrt{\frac{1}{4} + \frac{a(1-a)}{\lambda_r^2}} \tag{2.44}$$

The double root will however only be defined for positive values. The minus sign between the two terms can therefore be neglected. C_p will reach its maximum value when $a'(1-a)$ in equation (2.43) is greatest. Substituting the value of a' into $a'(1-a)$ and extracting λ_r yields:

$$\lambda_r^2 = \frac{(1-a)(4a-1)^2}{1-3a} \tag{2.45}$$

which defines the axial induction factor as a function of the local speed ratio at maximum power. If λ_r^2 then is substituted into equation (2.36) and (2.34) one obtain the angular induction factor for maximum power as a function of the axial induction factor.

$$a' = \frac{1-3a}{4a-1} \tag{2.46}$$

By differentiation of equation (2.45) one obtains a relationshup between $d\lambda_r$ and da at maximum power production.

$$2\lambda_r d\lambda_r = \{\frac{6(4a-1)(1-2a)^2}{(1-3a)^2}\}da \tag{2.47}$$

Substituting that into equation (2.18) gives:

$$C_{p,max} = \frac{24}{\lambda^2}\int_{a_1}^{a_2}\{\frac{(1-a)(1-2a)(1-4a)}{1-3a}\}^2 da \tag{2.48}$$

Note that the expression only is defined for values of $a_1 > 0,25$ and $a_2 < 1/3$. a_1 corresponds to $\lambda_r = 0$ and a_2 to $\lambda_r = \lambda$.

The result is, see [Eggleston and Stoddard 1987]

$$C_{p,max} = \frac{8}{729\lambda^2}\frac{64}{5}\{x^5 + 72x^4 + 124x^3 + 38x^2 - 63x - 12ln(x) - 4x^{-1}\}_{x=(1-3a_2)}^{x=0,25} \tag{2.49}$$

where $x = (1-3a)$.

The power coefficient from the two previous models have been plotted in figure 2.4.

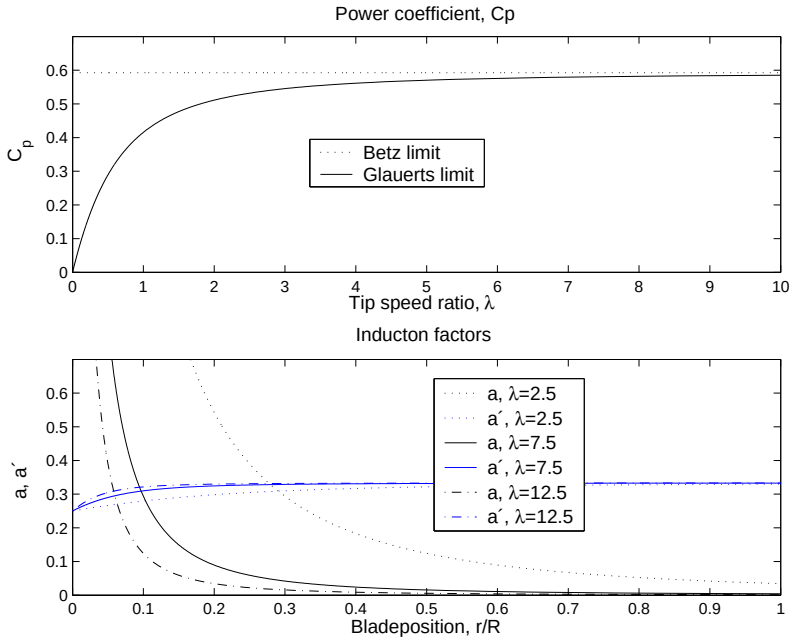

FIGURE 2.4. Power coefficient and induction factors

When the rotation of the wake is not included, C_p is constant at $16/27 \approx 0,59$ for all tip speed ratios, this value is generally expressed as Betz limit. When the wake rotation is considered, the value of the power decreases when the tip speed ratio decreases, here expressed as Glauerts limit.

The tip speed ratio for the wake rotation model has also been plotted for different blade positions in figure, 2.4. The Betz axial induction factor, $a = 1/3$ does correspond quite well to the wake rotation model when the distance from the hub is quit large, at least for quit large tip speed ratios.

2.2.3. *Far wake pressure*

In previous models, the momentum balance is taken over a stream tube of the form seen in figure 2.1 which in principle is not possible. This is however common in literature. In reality, the pressure varies on the mantle area of the stream tube. It is however possible to overcome this by considering a much larger stream tube, where the pressure disturbance will decay as $\frac{1}{r^2}$. Normally this effect is neglected since it is small.

2.2.4. *Blade element model*

So far we modelled the turbine without considering the blades themselves. In the momentum theory the forces were derived by considering conservation of momentum.

In the blade element method the forces are expressed as functions of lift and drag coefficients. This method will however also consider the angle of attack. The basic idea is to split the blades into N sections. Thereafter the forces are calculated at each element. The total force will be given by the sum of all elements of one blade multiplied by the number of blades.

There is however still a number of assumptions and simplifications that has to be made.

- First, the aerodynamic interaction between the blades is neglected.
- Second, the forces are only determined by the lift and drag characteristics of the airfoil shape of the blades.
- This model does also assume that the wind is orthogonal to the plane of rotation. It is, however, possible to make the model more general so it can handle different yaw angles.

To model the forces correct one has to analyze the different forces involved carefully. When considering the different forces, three different system are defined, green, red and blue. See figure 2.5.

The green system represents the wind velocity. The relative wind, U_{rel}, to the blade is the result of axial and angular contributions. The axial velocity at the blade is the free stream velocity retarded to $U_\infty(1-a)$ because of the induction discussed in section 2.2.2. The angular contribution is a combination

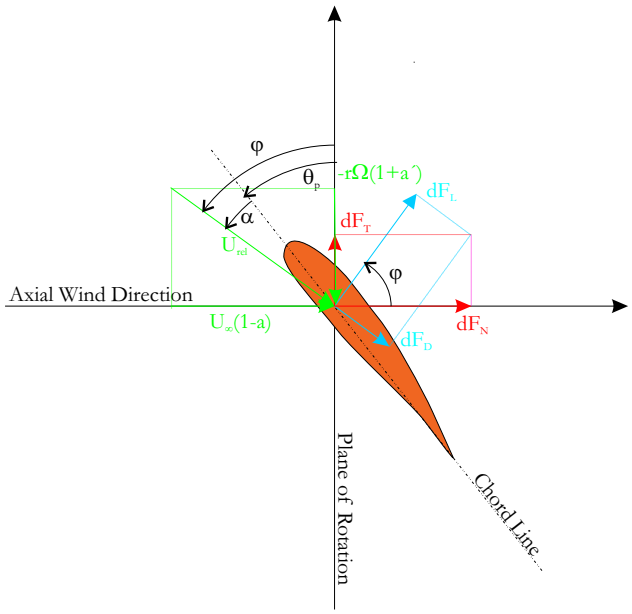

FIGURE 2.5. Definition of forces, velocities and angles.

of angular velocity $r\Omega$ and angular induction $a'r\Omega$ also discussed in section 2.2.2.

The blue system is the blade forces orthogonal and parallel to the local wind direction. dF_L represents the lift force and dF_D represents the drag force, both at section N. The red system is the same forces as in the blue system only transformed to be orthogonal and parallel to the plane of rotation. Therefore, the dF_T force represents the force contribution in angular direction from section N, i.e. useful torque. The dF_N force will in this case not lead to any useful energy. It will give a thrust force to the tower.

The section pitch angle is represented by θ_p. (It is composed of the blade root pitch angle and the local twist angle.)

ϕ represents the relative wind angle, i.e. the section pitch angle plus the angle of attack, $\theta_p + \alpha$,where α is the angle of attack.

From figure 2.5 one can determine the following relations:

$$\tan\phi = \frac{U_\infty(1-a)}{\Omega r(1+a')} = \frac{1-a}{(1+a')\lambda_r} \tag{2.50}$$

$$U_{rel} = \frac{U_\infty(1-a)}{\sin\phi} \tag{2.51}$$

$$dF_L = C_l \frac{1}{2} \rho U_{rel}^2 c dr \tag{2.52}$$

$$dF_D = C_d \frac{1}{2} \rho U_{rel}^2 c dr \tag{2.53}$$

$$dF_N = dF_L \cos\phi + dF_D \sin\phi \tag{2.54}$$

$$dF_T = dF_L \sin\phi - dF_D \cos\phi \tag{2.55}$$

The total force will be the sum of the contributions from all sections multiplied by the number of blades, B. For one section at radius r the normal force, i.e. the force which will lead to a thrust force, will be:

$$dT = B \frac{1}{2} \rho U_{rel}^2 (C_l \cos\phi + C_d \sin\phi) c dr \tag{2.56}$$

The torque, Q, from a section at radius r will be:

$$dQ = B r dF_T = B \frac{1}{2} \rho U_{rel}^2 (C_l \sin\phi - C_d \cos\phi) c r dr \tag{2.57}$$

Equation (2.56) and (2.57) gives the torque and thrust of the turbine. If these equations will be combined with the momentum theory one will obtain the blade element momentum model which will discussed in section 2.2.6.

2.2.5. *Blade shape*

Before moving on to the blade element momentum method which can be considered quit complex, a simpler approximation for the blade shape is performed. This method will derive the relation between the blade shape and performance for the optimum Betz rotor. The method uses the following assumptions:

- The wake rotation is neglected, i.e. the a' is set to zero.
- There is no drag, $C_d = 0$.
- The effects of finite number of blades is neglected.
- The induction factor a is 1/3 in each annular stream tube for Betz optimal rotor.

To use this design method, the tip speed λ, the number of blades B, the radius R and an airfoil with known lift and drag coefficients as function of angle of attack must be chosen.

The angle of attack will be chosen so the assumption $C_d = 0$ becomes as good as possible, i.e. the C_d/C_l term is minimized. With $a = 1/3$ one gets from momentum theory and equation (2.33):

$$dT = \frac{8}{9}\rho U_\infty^2 \pi r dr \tag{2.58}$$

and from blade element theory the equation (2.56), with $C_d = 0$ becomes:

$$dT = B\frac{1}{2}\rho U_{rel}^2 (C_l \cos\phi) c dr \tag{2.59}$$

By using equation (2.51) with $a = 1/3$, U_{rel} can be expressed as:

$$U_{rel} = \frac{2U_\infty}{3\sin\phi} \tag{2.60}$$

If eq. (2.58), (2.59) and (2.60) are combined one gets:

$$\frac{C_l B c}{4\pi r} = \tan\phi \sin\phi \tag{2.61}$$

Then, to relate a, a´ and ϕ, equation (2.50) is used and can now be expressed as.

$$\tan\phi = \frac{2}{3\lambda_r} \tag{2.62}$$

When combining eq. (2.61) and (2.62) and using that $\lambda_r = \lambda(r/R)$, it is possible to express ϕ and c as:

$$\phi = \tan^{-1}\frac{2}{3\lambda_r} \tag{2.63}$$

$$c = \frac{8\pi r \sin\phi}{3BC_l\lambda_r} \tag{2.64}$$

Betz optimum blade design can now be calculated using equation (2.63) and (2.64) together with geometrical relations from figure 2.5.

It can be seen that the blade design for an optimal Betz design have increasingly large chord and twist angle as one gets closer to the hub.

2.2.6. *Blade element momentum BEM model*

This section will combine the results from the momentum and blade element method. If the forces from momentum theory and blade element theory are set to be equal. One can derive the flow conditions for a turbine design.

The analysis starts by considering equations derived both for momentum theory with wake rotation and blade element theory.

From the momentum theory:

$$dT = 4a(1-a)\rho U_\infty^2 \pi r dr \tag{2.65}$$

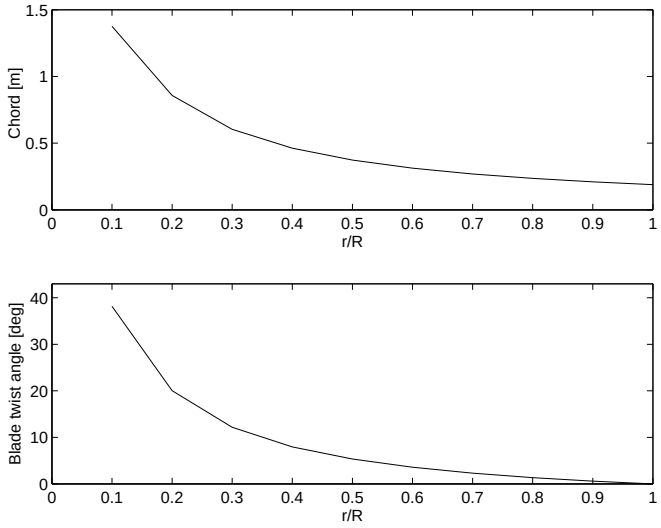

FIGURE 2.6. Betz Design of a wind turbine blade

$$dQ = 4a'(1-a)\rho U_\infty \Omega \pi r^3 dr \tag{2.66}$$

and from blade element theory:

$$dT = B\frac{1}{2}\rho U_{rel}^2 (C_l \cos\phi + C_d \sin\phi) c dr \tag{2.67}$$

$$dQ = B r dF_T = B\frac{1}{2}\rho U_{rel}^2 (C_l \sin\phi - C_d \cos\phi) c r dr \tag{2.68}$$

The relative wind velocity in the equations from the BE-method can now be expressed in terms of the free stream velocity, using equation (2.51):

$$dT = \sigma'\pi\rho\frac{U_\infty^2(1-a)^2}{\sin^2\phi}(C_l \cos\phi + C_d \sin\phi) r dr \tag{2.69}$$

$$dQ = \sigma'\pi\rho\frac{U_\infty^2(1-a)^2}{\sin^2\phi}(C_l \sin\phi - C_d \cos\phi) r^2 dr \tag{2.70}$$

where σ' is the local solidity, defined by:

$$\sigma' = \frac{Bc}{2\pi r} \tag{2.71}$$

In the calculation of induction factors, a and a', accepted practice is to set C_d equal to zero, [Wilson and Lissaman]. This simplification introduces

negligible errors for airfoils with low drag coefficients, [Manwell et al]. Equation (2.66) from momentum theory and (2.70) from the BE-theory will now, with $C_d = 0$, become:

$$dQ = 4a'(1-a)\rho U_\infty \Omega \pi r^3 dr \tag{2.72}$$

$$dQ = \sigma' \pi \rho \frac{U_\infty^2 (1-a)^2}{\sin^2 \phi} C_l \sin\phi r^2 dr \tag{2.73}$$

In the momentum theory one do, however, assume infinitely number of blades. Therefore, when neglecting this, an approximation is made when equations from momentum theory is set to equal with equations from the blade element theory. This does, however, give small errors since the a' is small at the tip and at the root where it is larger, it does have small impact because of a small torque. When the equations describing the torque, from momentum and blade element theory, are set to be equal, the result is:

$$\frac{a'}{1-a} = \frac{\sigma' C_l}{4\lambda_r \sin\phi} \tag{2.74}$$

When doing the same for the thrust force one gets:

$$\frac{a}{1-a} = \frac{\sigma' C_l \cos\phi}{4\sin^2\phi} \tag{2.75}$$

From equation (2.74) and (2.75) one can get the following results:

$$C_l = 4\sin\phi \frac{\cos\phi - \lambda_r \sin\phi}{\sigma'(\sin\phi + \lambda_r \cos\phi)} \tag{2.76}$$

$$a = \frac{1}{1 + 4\sin^2\phi / \sigma' C_l \cos\phi} \tag{2.77}$$

$$a' = \frac{1}{4\cos\phi/\sigma' C_l - 1} \tag{2.78}$$

$$\frac{a}{a'} = \frac{\lambda_r}{\tan\phi} \tag{2.79}$$

Equation 2.79 can be given a geometrical interpretation according to figure 2.7. The approximation of neglecting effects from discrete number of blades (tip effects) does only hold when the angle, A, between the relative and induced velocity in figure 2.7 is orthogonal.

When not neglecting the effect of discrete number of blades in the momentum theory, equation 2.65 must be multiplied by the Prantl's tip correction function, F.

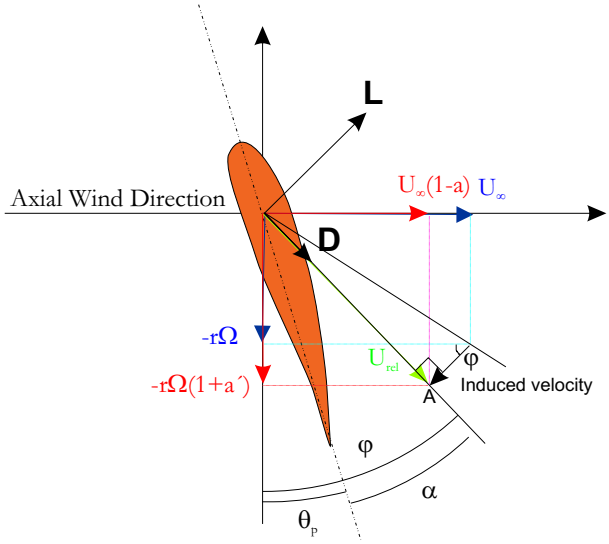

FIGURE 2.7. Geometrical interpretation of equation 2.79.

$$F = \frac{2}{\pi} arccos(e^{-f}) \tag{2.80}$$

where f is defined as:

$$f = \frac{B}{2} \frac{R - r}{R sin\phi_{tip}} \tag{2.81}$$

where B is the number of blades, R the turbine radius, ϕ_{tip} the tip pitch angle. A description about the derivation of the Prantl's tip correction function is given in section 3.5.

When introducing Prantl's tip correction, equation 2.75 is modified to:

$$\frac{a}{1-a} F = \frac{\sigma' C_l \cos\phi}{4 \sin^2\phi} \tag{2.82}$$

This expression now contains all information needed for the blade design if equation 2.79 is used as a relation between a and a' with approximations discussed above.

2.3. Performance

To determine the performance, C_p, is calculated. From equation (2.72) the torque developed by the blade elements of span-wise length dr is:

$$dQ = 4a'(1-a)\rho U_\infty \Omega \pi r^3 dr \tag{2.83}$$

The drag has however been excluded in this equation. When calculating the torque caused by drag, the drag must however be included. Therefore, the drag term is added to equation (2.83), see equation (2.68).

$$dQ = 4a'(1-a)\rho U_\infty \Omega \pi r^3 dr - B\frac{1}{2}\rho U_{rel}^2 c C_d \cos(\phi) r dr \tag{2.84}$$

The complete rotor will then develop a total torque Q of; [Burton et al]

$$Q = \frac{1}{2}\rho U_\infty^2 \pi R^3 \lambda \left[\int_0^R \left(\frac{r}{R}\right)^2 \left[8a'(1-a)\frac{r}{R} - \frac{U_{rel}}{U_\infty}\frac{B\frac{c}{R}}{\pi} C_d (1+a') \right] d\left(\frac{r}{R}\right) \right] \tag{2.85}$$

The total power developed by the rotor is the total torque multiplied by the angular velocity of the rotor, i.e. $Q\Omega$:

$$C_p = \frac{Q\Omega}{\frac{1}{2}\rho U_\infty^3 \pi R^2} \tag{2.86}$$

Solving the equations from the blade element momentum theory, for a specific design, yields the power and torque coefficients which are functions of the tip speed ratio.

In figure 2.8 a typical performance curve for a modern high-speed wind turbine is shown.

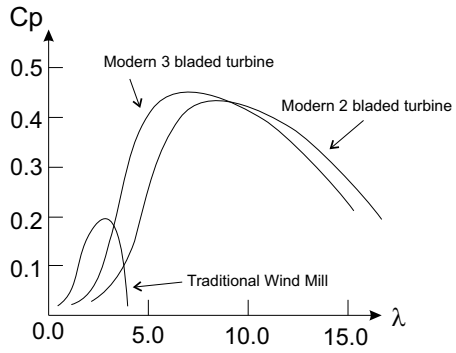

FIGURE 2.8. Cp values for a traditional wind mill compared with modern 2 and 3 bladed turbines.

The maximum power occurs when a, which normally varies with radius, approaches the Betz condition of $a = \frac{1}{3}$.

2.4. Breakdown of the validity of the momentum theory

For heavily loaded turbines, when a and a' are high, the momentum and vortex theories cease to be applicable. This is because the momentum theory predicts a reversal of the flow in the wake. Since that situation cannot occur, the wake becomes turbulent and starts to entrain air from outside the wake by a mixing process which re-energizes the slow moving air which has passed through the rotor disk.

When comparing results from momentum theory with measurements, the following approximation can be made of the thrust force coefficient. Let C_{T1} be the empirical value of C_T when $a = 1$. The empirical correction should be tangential to the momentum theory at the transition point. The equation for the empirical correction is, [Freris].

$$C_T = C_{T1} - 4(\sqrt{C_{T1}} - 1)(1 - a) \tag{2.87}$$

and the value of a at the transition point is:

$$a_T = 1 - 0.5\sqrt{C_{T1}} \tag{2.88}$$

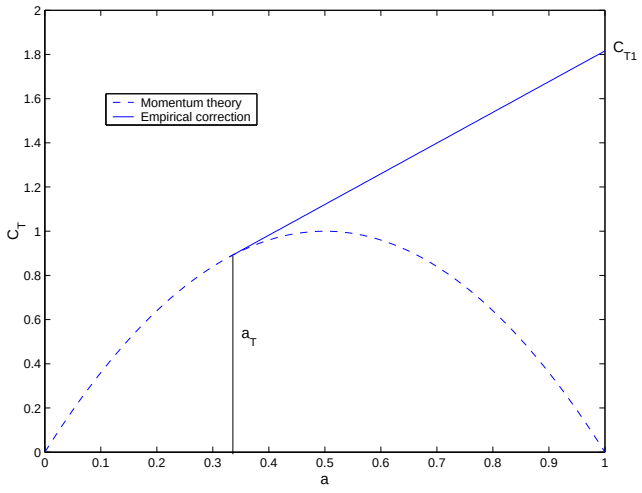

FIGURE 2.9. Empirical correction to the momentum theory, $C_{T1} = 1,816$

C_{T1} must lie between 1.6 and 2. According to Anderson, [Anderson], C_{T1} should be 1.816 for the best fit.

CHAPTER 3

Wake Structure

This chapter describes the effects of a discrete number of blades. When the fluid passes trough the turbine some particles are interacting with the rotor blades while some pass between them. Therefore, the loss of momentum will differ between the particles in the fluid and the induced velocity will vary around the disk.

To model the wake and include effects from discrete number of blades, the wake behind the rotor can be represented by a vortex model. With a vortex system the load can be calculated when the geometry of the wake is known. In the case of a slender wing, the lifting line model derived by Prantl can be used.

3.1. Vorticity

The vorticity is defined as:

$$\zeta = \nabla \times \vec{v} \tag{3.1}$$

A vortex can exist freely, as fluid rotating about a line which can be curved or strait. The structure of the vortex is such that the tangential velocity is inversely proportional to the distance from the vortex centre. This implies that the velocity at the centre is infinite. This can of course not be true. The vortex core is made up of a mass of fluid with a rigid body rotation, see figure 3.1.

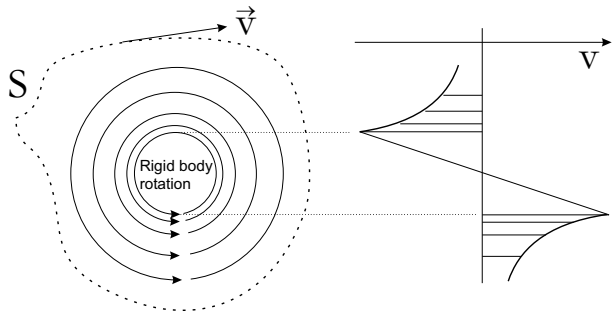

FIGURE 3.1. Vortex structure and integration path.

The radius of the core depends upon the circumstances of the flow situation. A vortex will move freely with the general fluid motion, although it will of course contribute to the motion. The vortex can only arise in a viscous fluid. However, if a vortex would arise in a inviscid fluid, it would require no input of energy to sustain and therefore also have infinite tangential velocity at the core. The core of a vortex must terminate at each end on a solid body or it must form a closed loop. In idealized two-dimensional flow, a vortex core is assumed to be infinitely long and strait in the third dimension.

A vortex bound to a finite airplane wing or a wind turbine blade cannot simply terminate at the wing/blade tip or at the blade root. Therefore, vortex trails from each tip, or for the wind turbine also at the blade root. Theoretically, they are stretched to infinity but, in practice, they are dissipated by viscosity some distance behind the wing or blade, see figure 3.2.

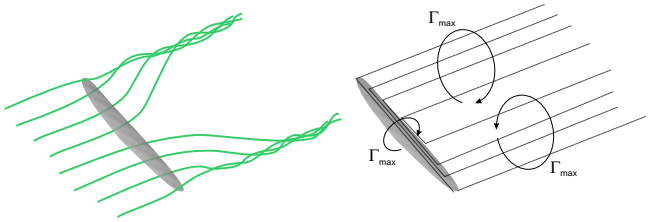

FIGURE 3.2. Left: Vortex trails from a wing. Right: Vortex trails represented by vortex lines.

A number of studies been done in the vortex area. Dispersive and dissipative errors in numerical solutions of flow field describing a vortex that advects in constant free stream been studied in detail by Efraimsson et al. [Efraimsson et al]. The long time development of an isolated wing tip turbulent vortex has been studied by RANS computations by Wallin and Girimaji, [Wallin, Girimaji].

3.2. Circulation

A useful quantity in the context of induction theory is the circulation, Γ. The circulation is defined as the vorticity integrated over an open surface bounded by S:

$$\Gamma = \oint \vec{v} dS \tag{3.2}$$

where $\vec{v}$ is the velocity along the curve S which encloses the vortex, see figure 3.1.

Kutta and Joukowski showed that the lift per unit span on an airfoil is proportional to the circulation bound to the wing/airfoil, [Mast].

$$\vec{L} = \rho \vec{U}_\infty \times \vec{\Gamma} \tag{3.3}$$

3.3. Helmholtz' theorem

Theoretically, the bound circulation on the blade is equal to the circulation behind the blade, i.e. in the wake. For inviscid flows, the sum of the tip and root vortex should be zero, that is however not the case for viscous flows.

The tip and root vortex do however, both for inviscid and viscous flows, have different sense of rotation, i.e. different signs of the circulation. A steep decline of circulation toward the tip will lead to a rapid concentration of the vortex at the tip. (Occurring a few chords behind the tip) The sign of the circulation gradient along the blade will also determine the sense of rotation of the vortex behind the blade. This means that if there is more than one region with a negative gradient, there will be more vortices than the tip and root vortex, see figure 3.3:

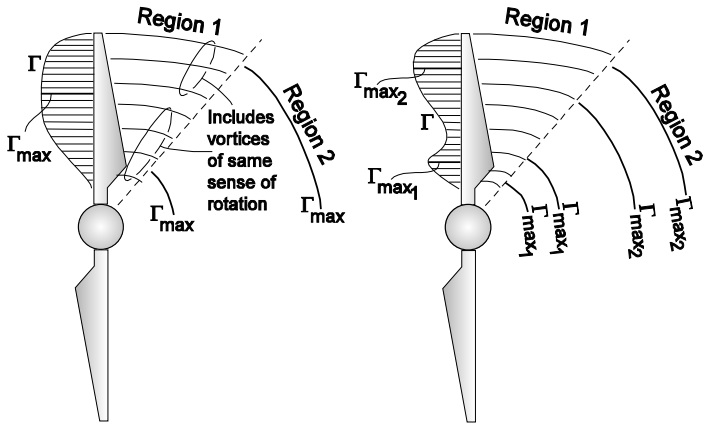

FIGURE 3.3. Trailing circulation modeling

The figure 3.3 shows two different distributions of circulation. The left shows a distribution with only one area of positive and negative gradient of the circulation function. Therefore, it will also only be one area of positive and negative rotations. The right figure does, however, show a distribution with two areas with negative and positive gradient of the circulation function. That distribution will give four vortices instead of two. The figure also shows an area trailing the blade where the concentrated vortices are formed. The size of that area is illustrated by the rapidity by with full circulation strength is attained, as demonstrated in figure 5.18, where the tip vortex formation is seem to have occurred where the plotted curve begins, i.e. at about 30° of azimuthal travel after blade passage. The root vortex concentration occurs more slowly because the radial circulation gradient is lower than at the tip.

The vortex is formed during a short time behind the blade, region 1 in figure 3.3. In inviscid theory the circulation for the tip and root vortex should both be equal to the maximum circulation along the blade. An explanation of that is given in figure 3.2, where one can see that the maximum bound circulation at the wing is reached when including all vortex lines along the wing. The circulation in the wake must therefore also correspond to that value

when considering all vortex lines leaving the wing. The vortex lines do however in reality interact as shown in the left part of figure 3.2. When considering a wind turbine blade, we have the same basic behaviour but instead of two tip vortices, we have one root and one tip vortex from each blade.

In reality, the viscosity does, however, affect the vortices differently depending on the flow field. Therefore, it is not possible to make any conclusions about the dependence of the tip and root vortex other than that when neglecting viscosity, one would expect the sum of the circulation of the tip and root vortex to be approximately zero.

The tip vortices are shed into the wake in a continuous fashion and appear to emanate from a curtain radius which is slightly smaller than the radius of the turbine blade tips. (Difference between b and b´) The vortices also concentrate to a root vortex. Therefore it is of great interest to simulate the behaviour of the swirls and where the concentration toward the outer and inner vortex take place.

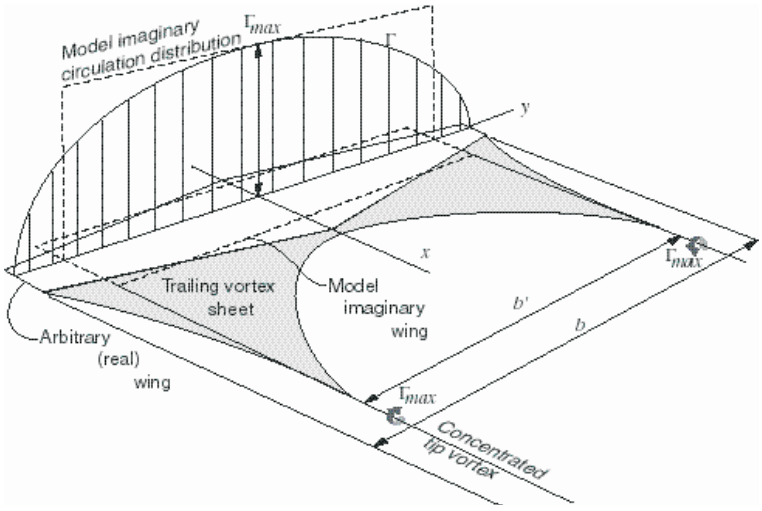

FIGURE 3.4. The figure shows where the tip vortex for an wing is located, [Montgomerie 2004a].

Figure 3.4 shows that when replacing the continuous distribution of the circulation by a constant distribution corresponding to the Γ_{max} value. The wing can be replaced by an imaginary one, which will have the same lift force as the physical one. The distance between the positions of the concentrated tip vortices equals the span, b´, of the outer edges of the imaginary wing. A similar but more complex theory can be applied to a wind turbine case.

3.4. Experimental results

Wake structures have been studied in experimental setups. To get an idea of the wake structure some experimental results are shown. In figure 3.5 the wake structure is visualized by smoke. One can then see the smoke trails when the smoke is sucked into the vortex core.

In figure 3.6 one can also see how the vortex spirals interact downstream and eventually pair up and desolve.

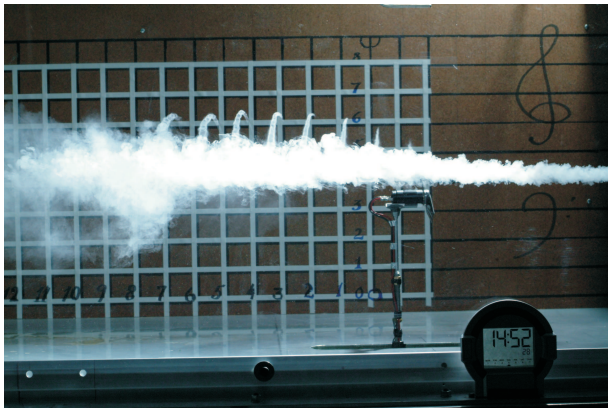

FIGURE 3.5. Wind tunnel measurement in wind tunnel LT5 at FOI, 2003, [Montgomerie, Dahlberg]

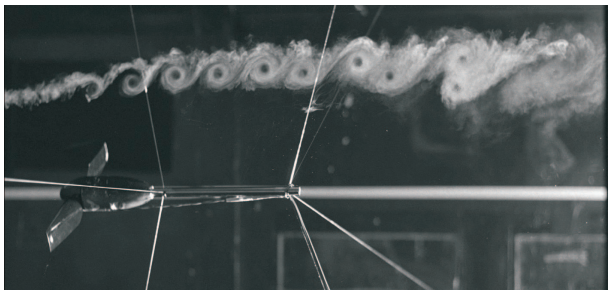

FIGURE 3.6. Wind tunnel measurement. [Alfredsson, Dahlberg]

Figure 3.7 shows a close up of the tip vortex, here illustrated by inserting smoke into the flow field. The blade is positioned, to the right, outside the picture. One relies that it is not trivial to model or simulate the complex behaviour of the wake structure.

FIGURE 3.7. Wind tunnel measurement in wind tunnel LT5 at FOI, 2003, [Montgomerie, Dahlberg]

Figure 3.8 shows how the tip and root vortices moves downstream. The rotational direction of each vortex is noted by an arrow. As discussed before, the circulation at the blades, in the wake, in both tip and root vortex, have the same value, because of Helmholtz' theorem, that states that for a inviscid fluid vortices in a homogeneous medium always form a closed loop. A vortex can only end in a surface, for example a tornado with the ground as a surface.

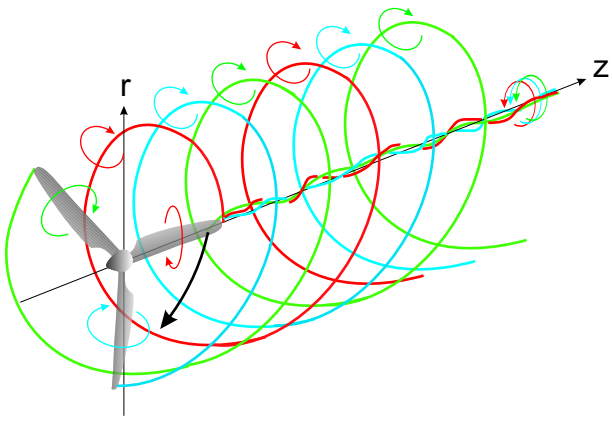

FIGURE 3.8. Since the blade tip follows a circular orbit it leaves a trailing vortex of a helical structure. The trailing tip vortex moves downstream.

3.5. Tip-losses

If the axial flow induction factor a is large at the blades position, the inflow angle ϕ will be small. The lift force in tangential direction will therefore also be small. The torque will then be reduced which means reduced power. This reduction does not only occur at the outermost part of the blades but is normally referred to as tip-losses. An interpretation of the inhomogeneous flow over the disc can be seen in figure 3.9.

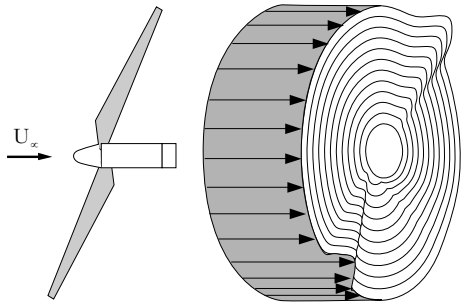

FIGURE 3.9. The figure shows the deceleration of the flow, which is not homogeneous over the disc. The maximum deceleration occurs on the blades themselves. The wake flow reflects the same effect. Therefore, the change of momentum flux (being equal to the rotor thrust) must be evaluated at some downstream location with an inclusion of the deformation. The direction of the vectors, illustrating the deceleration, in the figure is opposite to the physical direction.

In 1919 Lundwig Prandtl developed an ingenious approximation for the tip-loss factor. It yields a rather simple analytical formula. Prandtl's method was inspired by the fact that no particle can pass thought the vortex sheet. Prandtl replaces the sheet with solid discs moving with the wake velocity $U_\infty(1-a)$. See figure 3.10.

The theory only applies to a fully developed wake. The distance between each disc, d, is set to the flow direction pitch of the vortex sheets. The free stream air seems to tend to weave in and out between the discs. Prantl's tip-loss correction function, F, for the trust when using momentum theory is defined as:

$$F = \frac{2}{\pi} arccos(e^{-f}) \tag{3.4}$$

where f is defined as:

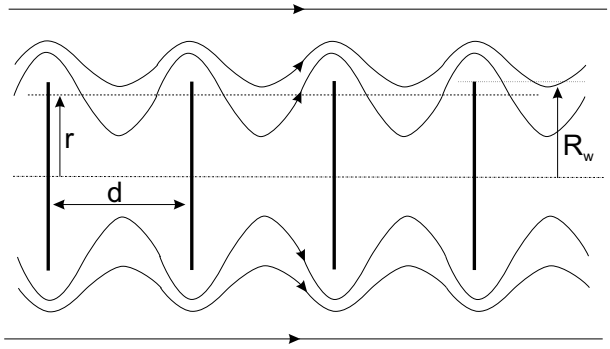

FIGURE 3.10. Prantl's tip loss approximation.

$$f = \frac{B}{2}\frac{R-r}{Rsin\phi_{tip}} \tag{3.5}$$

where B is the number of blades, R the turbine radius and ϕ_{tip} the tip pitch angle. F can be interpreted as the ration between the mean induced velocity in the flow annulus to the induced velocity at the blades.

For mathematical details of Prandtl's analysis, see Glauert [1935]

CHAPTER 4

Numerical Methods

This chapter deals with modern simulation methods based on numerical methods.

4.1. Actuator disc method

4.1.1. *Introduction*

This numerical method combines experiences from CFD (Computational fluid Dynamics) methods with experimental data by using airfoil data. The blades are here represented by volume forces representing the force distribution on the blades that act on the ambient air. This numerical approach to the actuator disc concept been developed by Sørensen and colleagues, [J.N.Sørensen, Myken], [N.N.Sørensen, Kock], [J.N.Sørensen, Shen, Munduate]. The main idea is to solve the flow past a rotor without resolving the boundary layer on the blades.

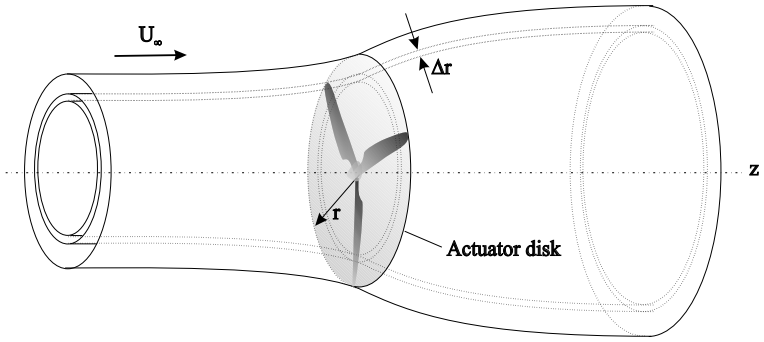

FIGURE 4.1. Actuator Disc Concept

The presence of the rotor is modelled through body forces found from local flow and airfoil data. Navies-Stokes equations are formulated as:

$$\frac{\partial u_i}{\partial t} + u_j \frac{\partial u_i}{\partial x_j} = -\frac{1}{\rho}\frac{\partial p}{\partial x_i} + f_{body,i} + \nu \frac{\partial u_j^2}{\partial x_j^2} \tag{4.1}$$

where f_{body} represents force extraction from the blades.

4.1.2. *Definitions*

The velocity notation according to figure 4.2 is introduced.

$$\tan\phi = \frac{U_\infty - W_z}{\Omega r + W_\theta} \tag{4.2}$$

$$a = \frac{W_z}{U_\infty} \tag{4.3}$$

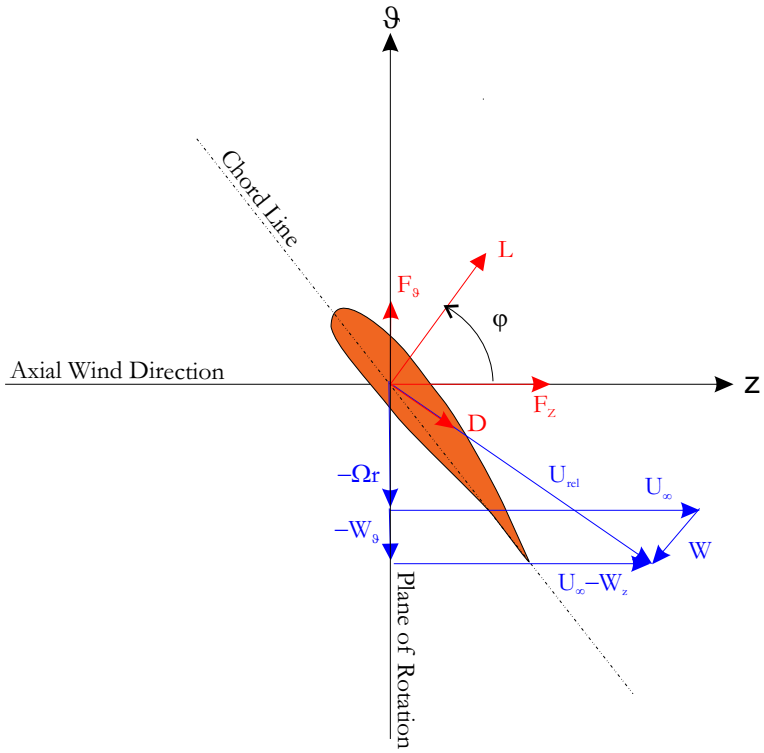

FIGURE 4.2. Velocity notation, compare with figure 2.5

$$a' = \frac{W_\theta}{\Omega r} \tag{4.4}$$

$$U_{rel}^2 = (U_\infty - W_z)^2 + (\Omega r + W_\theta)^2 \tag{4.5}$$

Lift and drag forces per span wise length are found from tabulated airfoil data as:

$$(\boldsymbol{L}, \boldsymbol{D}) = \frac{1}{2}\rho U_{rel}^2 cB(C_L \boldsymbol{e}_L, C_D \boldsymbol{e}_D) \tag{4.6}$$

where C_L and C_D are functions of α and Re. The unit vectors $\boldsymbol{e}_L$ and $\boldsymbol{e}_D$ are defined in the directions of lift and drag respectively. The Force per span wise unit length is written as the vector sum:

$$\mathbf{F} = \mathbf{L} + \mathbf{D} \tag{4.7}$$

with

$$F_z = L\cos\phi + D\sin\phi,\ F_\theta = L\sin\phi - Dcos\phi \tag{4.8}$$

Then,

$$\Delta T = F_z \Delta r,\ \Delta Q = F_\theta r \Delta r \tag{4.9}$$

From the blade element momentum theory we know that the reduction from free stream velocity throught the stream tube is $2W_z$ in the axial direction because of axial momentum balance and $2W_\theta$ in radial direction because of angular momentum correspondingly. Then, for each annular element:

$$\Delta T = 2W_z \Delta \dot{m} \tag{4.10}$$

$$\Delta Q = 2W_\theta r \Delta \dot{m} \tag{4.11}$$

The blade element momentum method does, as discussed before, rely on the following assumptions:

- Axial symmetry
- Inviscid flow
- The annular stream tubes are radially independent
- The influence from pressure forces on expanding stream tubes are neglected.
- Induced velocity on the disc equals half the induced velocity in the far wake

This method is still based on the same assumptions, the main difference between the methods is that the forces in the ACD method is based on measured local values.

4.1.3. *Applying forces*

Volume forces are introduced to connect the simulation with the experimental data used to represent the blades. The loading for an annular area of differential size is:

$$\mathbf{f} = \frac{\mathbf{dF}}{dA} = \frac{1}{2}\rho U_{rel}^2 \frac{cB(C_L\mathbf{e}_L + C_D\mathbf{e}_D)}{2\pi r} \tag{4.12}$$

where $\mathbf{f}$ is defined in cylindrical coordinates as:

$$\mathbf{f} = (f_r, f_\theta, f_z) \tag{4.13}$$

and the resulting volume force:

$$\mathbf{f}' = \frac{\mathbf{f}}{dz} \tag{4.14}$$

where the force components of **F** are determined from equations (4.2), (4.6) and (4.8).

4.1.4. *Numerical implementation*

For a full description and numerical implementation of this model, see [Mikkelsen], [Sørensen and Myken].

4.2. Actuator line method

4.2.1. *Introduction*

The main limitation in the actuator disc method is that the method distributes the forces evenly in the tangential direction of the actuator disc. The influence of the blades is therefore taken as an integrated quantity in the azimuthal direction. An extended three dimensional method, Actuator Line Method (ACL), has however recently been introduced by Sørensen and Shen [Sørensen, Shen]. The limitation in the Actuator Disc Method, where the influence of the blades is taken as an integrated quantity in the azimuthal direction, has now been overcome by using techniques where volume forces are distributed along lines representing each blade. A full CFD simulation would require a great number of nodes at the blades to resolve the boundary layer. With this method, node points could be saved at the blades. This method does therefore open new possibilities for turbine simulations with a well resolved wake. The drawbacks is on the other hand that the method still is based on tabulated data from which C_L and C_D are functions of α, therefore, they are dependent on the quality of these experimental data.

This method has recently been implemented, by Mikkelsen [Mikkelsen], into the EllipSys3D code. EllipSys3D is a general purpose 3D solver developed by N.N.Sørensen and Michelsen, [N. N. Sørensen], [Michelsen 1992], [Michelsen 1994]. The flow solver is a multi block, finite volume discretization of the Navier-Stokes equations in general curvilinear coordinates. The code is formulated in primitive variables, i.e. pressure and velocity variables, in a collocated storage arrangement. Rhie/Chow interpolation is used to avoid odd/even pressure decoupling.

The presence of the rotor is modelled through body forces found from local flow and airfoil data. Navies-Stokes equations are formulated as:

$$\frac{\partial u_i}{\partial t} + u_j \frac{\partial u_i}{\partial x_j} = -\frac{1}{\rho}\frac{\partial p}{\partial x_i} + f_{body,i} + \nu \frac{\partial u_j^2}{\partial x_j^2} \tag{4.15}$$

where f_{body} represents force extraction from the blades.

The numerical method use the 3rd order QUICK (Quadratic Upstream Interpolation for Convection Kinematics) method for the convective terms and 2nd order CDS (Central difference schemes) for the diffusive terms.

The calculation domain consists of a number of blocks with an equal amount of points in each direction and block. The node points are distributed non-equidistant. The block size together with the number of points in each block control how gradients are captured at critical positions.

The actuator line method can handle both straight and bent lines, yawed, coned and tilted flow situations. The following sub models could also be used to get a more realistic flow situation.

- Elastic modal method
- Tower model - dipole and source
- Dynamic stall - Øye model
- Boundary layer or wind shear - power law

These models, suited to dynamic events, will, however, not be discussed here, for a description, see [Mikkelsen].

The blade forces are determined in the same manner as for the actuator disc method, see equation (4.6). There is however some modifications because of the geometry. Figure 4.3 shows a coned rotor in a cylindrical coordinate system (r, Θ, z), with velocity components $\mathbf{U} = (U_r, U_\Theta, U_z)$. A local coordinate system, (s,n,τ), is introduced, where s is the span wise coordinate, n the direction normal to the cone at the blade and τ the tangential direction. The velocity components normal to the rotor are (U_n, U_Θ) where U_n is determined as:

$$U_n = U_z \cos\beta + U_r \sin\beta \tag{4.16}$$

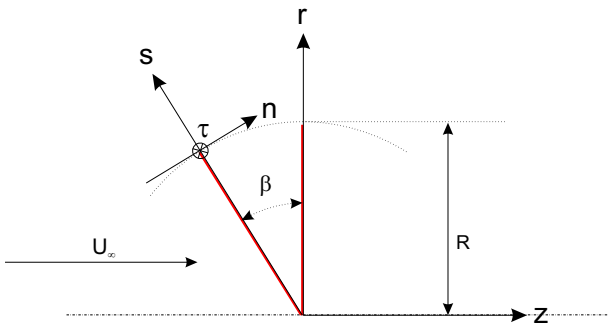

FIGURE 4.3. Geometry for coned actuator line

4.2.2. *Applying forces*

The aerodynamic forces that are distributed along the actuator line cannot only be applied in the actuator line points because of numerical discontinuity. The forces are therefore distributed among neighboring node points in a Gaussian

manner. This is done by taking the convolution of the computed load $\mathbf{f}_{r\theta z}$ and the regularization kernel η_ϵ.

$$\mathbf{f}_\epsilon^b = \mathbf{f}_{r\theta z}^b * \eta_\epsilon \tag{4.17}$$

where the regularization kernel is defined as:

$$\eta_\epsilon(p) = \frac{1}{\epsilon^3 \pi^{3/2}} e^{-(p/\epsilon)^2} \tag{4.18}$$

where p is the distance between cell centered grid points and points at the actuator line. The regularized force then becomes:

$$\mathbf{f}_\epsilon^{3D} = \sum_{b=1}^{B} \int_{s=0}^{R} \int_{-\infty}^{+\infty} \int_{-\infty}^{+\infty} \mathbf{F}^b(s) \eta_\epsilon(p^b) dn d\tau ds \tag{4.19}$$

Mikkelsen discovered that by using a 3D Gaussian smoothing results in inconsistencies near the tip region, [Mikkelsen]. Therefore, a 2D Gaussian distribution is used on a 2D-plane orthogonal to the actuator line. This smearing of the forces is therefore done globally, i.e. every node point at a plane orthogonal to the actuator line will be affected, even if the effect is negligible far from the line, because of the Gaussian function. The 3D Gaussian, if applied, would also increase the effective radius of the blade forces.

By taking the convolution of the computed load $\mathbf{f}_{r\theta z}$ and the 2D regularization kernel η_ϵ. The loading for the b'th actuator line is received as:

$$\mathbf{f}_\epsilon^{2D,b} = \mathbf{f}_{r\theta z}^b * \eta_\epsilon^{2D} \tag{4.20}$$

where the 2D regularization kernel is defined as:

$$\eta_\epsilon^{2D}(p) = \frac{1}{\epsilon^2 \pi} e^{-(p/\epsilon)^2} \tag{4.21}$$

The resulting loading is:

$$\mathbf{f}_\epsilon^{2D} = \sum_{b=1}^{B} \int_{-\infty}^{+\infty} \int_{-\infty}^{+\infty} \mathbf{F}^b(s) \eta_\epsilon^{2D}(p^b) dn d\tau \tag{4.22}$$

The 2D Gaussian distribution is controlled by the parameter ϵ. The choice of ϵ will also affect the numerical discontinuity at the tip, as a result of a 2D distribution. The choice of the value of ϵ will therefore be critical and will, especially, have great impact on the wake structure. This will be discussed further in section 5.4.

When the simulation starts, an initial velocity is introduced in the entire flow field, i.e. the free stream velocity. Then local velocities and angles of attack at blade positions are extracted. From tabulated airfoil data that originate

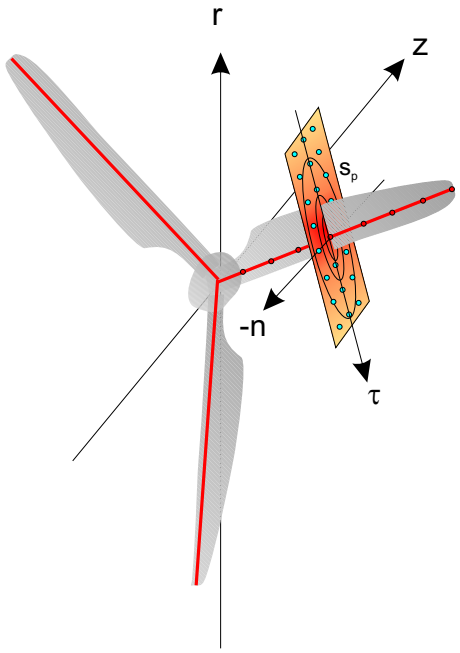

FIGURE 4.4. The figure shows the actuator line concept. Each blade is represented by a line with J_{rot} number of points. Forces at each actuator point is Gaussian distributed at all points, s_p, positioned at a plane orthogonal to the actuator line. The plane is infinite.

from full scale measurement one can then compute local volume forces. These volume forces are then imported into the flow field, at actuator line positions and to a plane orthogonal to the actuator line, controlled by the regularization kernel. Then next iteration begins. A new velocity field is reached and new local velocities and angles of attack are reached and so on.

4.3. Overview of CFD methods

The methods in the previous sections, ACD and ACL, are both based on the CFD method. They do, however, not use any turbulence model as is common when running CFD simulation. It is of course possible to do so, but for applications explained so far there is no real motivation to do so. This section will deal with other questions where turbulence models are important. This section is written as an orientation to problems in connection with CFD methods.

As discussed before, during recent years progress have been made in the field of numerical predictions of wind turbine blade aerodynamics. Because of

high Reynolds numbers, $O(10^6)$, the turbulence length and time scales span many orders of magnitude. Therefore, the Reynolds Averaged Navier-Stokes (RANS) methods are the most applied methods if a description of the whole flow field is desired. The problems that still need to be solved are:

- Growth and separation of the boundary layer
- Momentum transfer after separation

For attached flows, or thin shear flows, around blades. Steady RANS simulations with a proper turbulence model are known to perform well. Even if pressure gradients cause small regions of separation, unsteady RANS simulations can predict the flow properly. But for flows with massive separation, the flow becomes highly unsteady, both steady and unsteady RANS models fail to predict the correct separation leading to an overestimation of lift.

In CFD simulations using previously described models, i.e. ACD and ACL, the mechanical power has been predicted using CFD on a full wind turbine rotor. The results indicate that for low wind speeds, where the flow is mostly attached, the mechanical power is predicted well compared with measurements. For high wind speeds, on the other hand, the flow is over predicted. Here the flow is separated. [N.N.Sørensen, J.Johansen]

According to N. N. Sørensen and Johansen, [N.N.Sørensen, J.Johansen], this is primarily caused by two factors:

- First, the RANS simulation produces too much viscosity, causes a predicted lift which is too high.
- Secondly, the turbulence model does not correctly take into account the transport of momentum in the far field. This is due to the fact that turbulence modelled in a RANS simulation is assumed isotropic, which will force the flow to be kept artificially two-dimensional. In reality, the flow is definitely three-dimensional.

A new approach was introduced by N. N. Sørensen and Johansen, [N. N. Sørensen, J.Johansen]. As opposed to RANS, which is time averaged, LES, which is a space averaging, is used. Here the large eddies are resolved and only the smaller eddies are modelled assuming isotropic turbulence. Now, the correct three-dimensionality of the flow is predicted. The eddies close to the wall are however very small for Reynolds number relevant for wind turbine applications. Therefore, the LES is impractical solution method with respect to computational cost since very small grid cells and also small time steps would be required to resolve the small eddies. One way to circumvent the problems with LES is to combine the LES model with RANS. Use RANS model in the boundary layer but LES model in the far field. In this way the small attached eddies in the boundary layer will be modelled using RANS turbulence model and the detached eddies in the far field will be resolved using a LES approach. The new model is called "Detached-Eddy Simulation", (DES).

The CFD code EllipSys3D was used in the simulations. The SIMPLE algorithm is employed for the pressure/velocity coupling and solutions of the momentum equations are obtained using a second order upwind differencing scheme (SUDS) or a third order quadratic upwind interpolation scheme (QUICK). The RANS computations are employing the two-equation k - ω SST model by Menter [Menter]. The Detached-Eddy Simulation (DES) is based on the Spalart-Allmaras, (S-A) one-equation RANS model. [Spalart, Allmeras], which is reduced to a LES-like model in the farfield by a simple "switch".

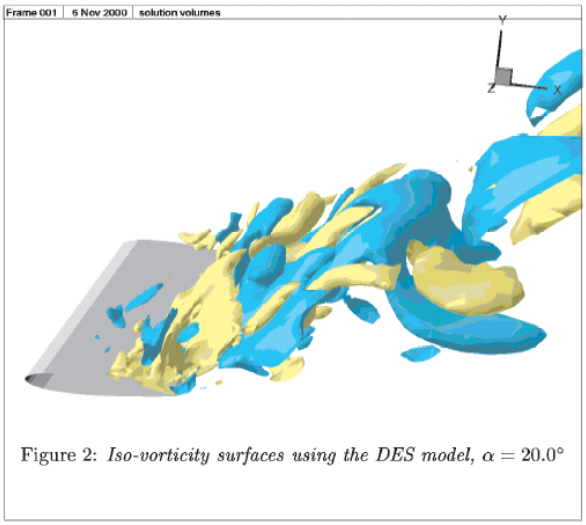

Figure 2: *Iso-vorticity surfaces using the DES model,* $\alpha = 20.0°$

FIGURE 4.5. DES Simulation performed by [N.N.Sørensen, J.Johansen]

Figure 4.5 shows the result from a DES simulation for a constant chord wing. The three-dimensionality using the DES model can be seen. The unsteady RANS simulation will however maintain two-dimensional even at highly separated flows. N. N. Sørensen and Johansen concluded that the DES model proposed by Spalart et al. [Spalart et al] captures the three-dimensionality of the flow physics well. The change from RANS to LES region has however to be investigated further.

4.4. Summary of classical and numerical models

The discussed models could be summarized as:

- Blade Element Momentum Method (BEM)
- Actuator Disk Method (ACD)
- Actuator Line Method (ACL)
- Full CFD simulation (CFD)

where all except the last, the CFD simulation, are based on tabulated airfoil data of some sort. To set up a full wake simulation using CFD methods where the blades, or at least one because of periodicity, must be fully resolved require a lot of computer recourses. As known, the evolution in that area does go fast, so who knows what the future might give.

Presented models do all have their advantages when looking at different aspects of the turbine. When creating new wind turbine design codes many fields of interest must be fulfilled. There are many complicated features that must be introduced as engineering methods in these codes. All these features are however not the topic of this report. A few examples are however introduced below.

4.4.1. *3D effects*

The flow at the blade tip- and root is three-dimensional. Due to centrifugal and Coriolis forces, the boundary layer at the root has a span wise direction while the flow just outside the layer is chord wise. This effect delays stall. Therefore, when considering this effect, one reaches higher lift forces compared to a 2d flow case.

This effect i commonly referred to as the Himmelskamp-effect. For further details about 3D effects, see [Snel et al].

4.4.2. *Dynamic wake and stall*

The induced velocities do not respond immediately to changes in loads. Therefore there is a time delay before effects from changes in loads take effect in the wake.

A time delay also exists in the separated boundary layer on an airfoil, when the angle of attack is changed fast.

Both these time dependent behaviours must also be implemented in engineering methods to describe the physical behaviour correctly, although this is outside the scope of this investigation.

CHAPTER 5

Results

5.1. Simulation setup

This section deals with choice of numerical method, numerical setup such as grid design, simulation cases etc.

5.1.1. *Numerical method*

Previous chapters show available simulation tools, since one of the aims in this project is to simulate the wake to make it possible to evaluate the wake behaviour. The simulation method "Actuator line" has been chosen since it gives possibilities to resolve the wake well and at the same time does not require a mesh of the blades themselves, which would require a lot of node points localized at the blades surfaces.

The Actuator line method captures effects in the ambient flow from the blades with the lowest computational requirements.

Simulations have been performed with the software EllipSys3D discussed in chapter 4.2. One can generally say that the performed computation is an inviscid DNS calculation since it uses a RANS code without turbulence models.

5.1.2. *Computer setup*

The simulation has been performed on a linux PC cluster at the Mechanical Department at DTU. The cluster has been explicitly developed for EllipSys3D and it has been built by Jess Michelsen. It contains 210 PC's with Linux Redhat 8 as an operating system. The cluster was taken into operation during the time of this project.

5.1.3. *Experimental data*

Since the actuator line method uses tabulated airfoil data from measurements, data with good quality must be used. Data from the turbine Tjaereborg have been used for all simulations in this project.

The Tjaereborg turbine was operational between 1988 and 1998. During these years extensive measuring and testing was performed on the turbine. The turbine was localized 9 km southeast of the city of Esbjerg in the western part of Denmark. Tjaereborg was a three-blade upwind horizontal axis turbine. The blade profiles were NACA 4412-43 with a blade length of 29 m giving a rotor diameter of 61 m. The chord length was 0.9 m at the tip, increasing lineary to 3.3 m at hub radius 6m. The blades are twisted 1° per 3m. The tip speed was 70.7 m/s and the rotor solidity was 5,9%. The rated power is 2 MW where the output was controlled by a continuously variable pitch operating between 0 and 35 degree in production mode. The hub height is 60 m. [Tjaereborg Data]

5.1.4. *Initial and boundary conditions*

The performed simulations only deals with axial flows. Therefore, it is possible to reduce the mesh to a 120-degree slice with periodic boundary conditions to account for the rest of the required cylinder volume.

All simulations were performed at operational conditions corresponding to a free stream velocity of 10 m/s. The initial velocity is therefore set to 10 m/s. The actuator line was fixed in the mesh. The rotational reference frame is created by an angular velocity at boundaries. The simulations are valid for steady conditions only. No coning of the blades was simulated in these computations.

5.1.5. *Mesh*

EllipSys3D is parallelized and uses MPI. EllipSys3D can, however, only handle blocks with the same number of nodes on each block edge or side. The distribution on each side of the block boundaries can, however, be nonlinear.

The mesh was created as a 5-block mesh to be able to capture large gradients in the wake.

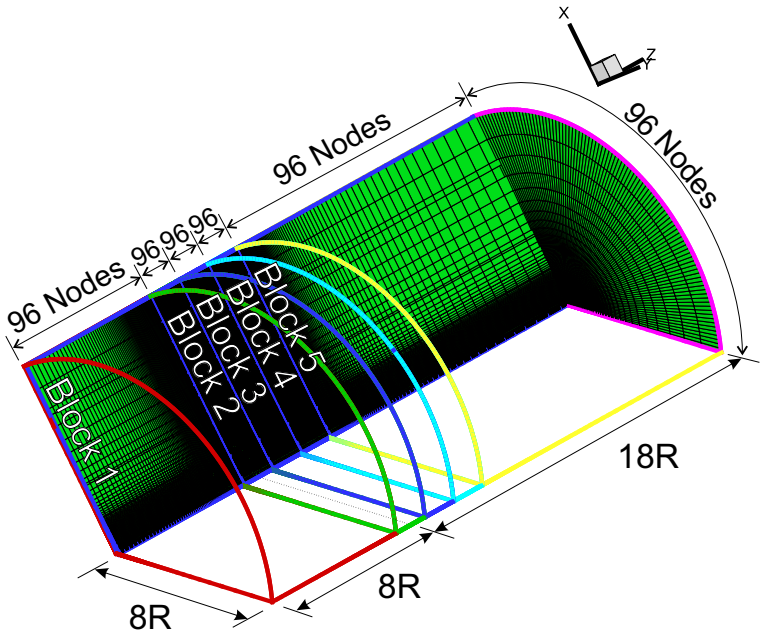

FIGURE 5.1. The figure shows the 5-block mesh and the distribution of the nodes. There are 96 nodes on each block side. In total this mesh contains $96^3 \cdot 5 \approx 4.4 \cdot 10^6$ nodes.

Figure 5.1 shows how the mesh is constructed. The aim is to resolve the wake as faithfully as possible. Block number 2, 3 and 4 are therefore thin in the z-direction to compress the node distance in the downstream direction. Blocks 2, 3 and 4 are equidistant in the z-direction. Blocks 1 and 5, including inlet and outlet, have a non-equidistant mesh in the z-direction. Here, the nodes are concentrated toward the turbine. In the radial direction, all blocks use the same densification toward the centerline. The actuator line is positioned in block 2, at the centre line and at 8 radii from the inlet.

5.1.6. *Sensitivity*

To evaluate the sensitivity of the grid four different meshes with different resolutions were constructed; 48, 64, 80 and 96 nodes on each block side. The total number of node points are then; $5.5 \cdot 10^5, 1.3 \cdot 10^6, 2.6 \cdot 10^6$ and $4.4 \cdot 10^6$.

To be able to evaluate the sensitivity of the Gaussian smearing function, three different values of parameter ϵ were simulated.

The sensitivity of the Reynolds Number has also been studied. Six different cases of Reynolds number been simulated, see figure 5.2. The effect of different Reynolds number will be discussed more thoroughly in chapter 5.2.6.

Case name	Mesh[1]	ε	Gauss	Re[2]	Prantl
T48Bk5TyE1D2	48	1	2d	$3{\cdot}10^6$	Yes
T48Bk5TyE15D2	48	1.5	2d	$3{\cdot}10^6$	Yes
T48Bk5TyE2D2	48	2	2d	$3{\cdot}10^6$	Yes
T64Bk5TyE1D2Re4	64	1	2d	$3{\cdot}10^6$	Yes
T64Bk5TyE1D2Re5	64	1	2d	$6{\cdot}10^6$	Yes
T64Bk5TyE15D2Re4	64	1.5	2d	$3{\cdot}10^6$	Yes
T64Bk5TyE2D2Re4	64	2	2d	$3{\cdot}10^6$	Yes
T80Bk5TyE1D2Re4	80	1	2d	$3{\cdot}10^6$	Yes
T96Bk5TyE1D2Re1	96	1	2d	$3{\cdot}10^3$	Yes
T96Bk5TyE1D2Re2	96	1	2d	$3{\cdot}10^4$	Yes
T96Bk5TyE1D2Re3	96	1	2d	$3{\cdot}10^5$	Yes
T96Bk5TyE1D2Re4	96	1	2d	$3{\cdot}10^6$	Yes
T96Bk5TyE1D2Re5	96	1	2d	$6{\cdot}10^6$	Yes
T96Bk5TyE1D2Re6	96	1	2d	$15{\cdot}10^6$	Yes
T96Bk5TyE15D2Re4	96	1.5	2d	$3{\cdot}10^6$	Yes
T96Bk5TyE2D2Re4	96	2	2d	$3{\cdot}10^6$	Yes

1, Nodes on each block side
2, Based on turbine radius

FIGURE 5.2. Case table

All simulations have been performed with a 2d Gaussian distribution.

Mikkelsen argues that the Prantl's tip correction should be left out since the 3D effect leading to tip losses is included in this method, [Mikkelsen]. It has, however, later been shown that more accurate results have been obtained when Prantl's tip correction is included. [Private discussion with Sørensen and Mikkelsen] This shows that the 3D effects leading to Prantl's tip losses are not included in the actuator line method itself. The correction by Prantl was included in these simulations. No efforts have been made to investigate this further. However, this is not scientific correct practice.

5.2. Simulation results

This section gives an overview of the results from the simulations.

5.2.1. *Pressure distribution*

Figure 5.3 illustrates the actuator line with color coding for levels of the force distribution. The contours between iso surfaces correspond to the pressure levels according to the legend. The blade actuator line representation is rotated 30°, out of the pressure distribution plane, in the direction of the viewer. It, therefore, appears unexpectedly short in relation to the tip vortex train.

The figure shows the pressure build up in front of the turbine. The vorticity spiral can be identified by the low pressure areas downstream of the actuator line.

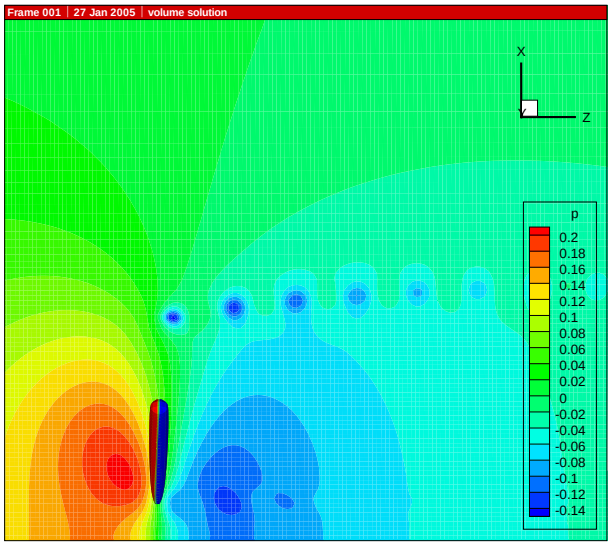

FIGURE 5.3. Pressure distribution for the 96 point mesh simulation 30° after blade passage, $Re = 3 \cdot 10^6$ (Re4).

5.2.2. *Velocity distribution*

Figure 5.4 illustrates the actuator line with an iso surface of the force distribution. The contour on that iso surface is the streamwise velocity distribution. The plane, showing the velocity distribution, is rotated 30° from the plane containing the actuator line also in this plot. The figure therefore shows the actuator line 30° in front of the plane showing the velocity distribution.

The figure shows the axial velocity distribution. The value 1 in the legend corresponds to the free stream velocity, i.e. 10 m/s. Upon magnification of selected details, it is possible to see that the rotation of the vortices are in clockwise direction. The velocity in the wake is also reduced as expected.

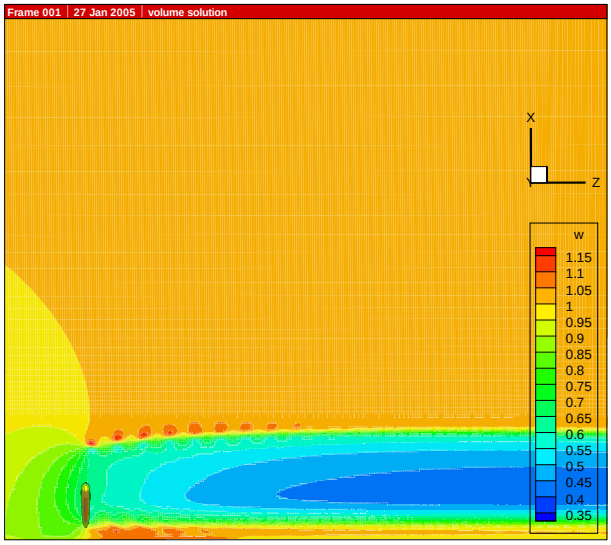

FIGURE 5.4. Streamwise velocity distribution for the 96 mesh simulation 30° after blade passage, $Re = 3 \cdot 10^6$ (Re4).

In figure 5.4 It is possible to see that the velocity in the centre line, i.e. the root vortex, is high compared to the mean wake velocity. This is partly because the nacelle is not present in this simulation. The flow field behind a real turbine does, however, also have a root vortex which may accelerate the flow. This have been varified by testing at FOI, [Dahlberg]. The correct physical behaviour might therefore represent real flow.

5.2.3. *Vorticity*

Figure 5.5 shows an iso surface of the vorticity with a pressure distribution on the iso surface. The x=0-plane also shows the pressure distribution. The y=0-plane shows the streamwise velocity distribution.

By choosing the value of the parameter for the vorticity, the "vortex spiral" can be identified.

5.2.4. *Position of the cores*

The position of the centre of the vortex cores was extracted from the flow field. The result shows that the position of the cores does not depend on the smearing

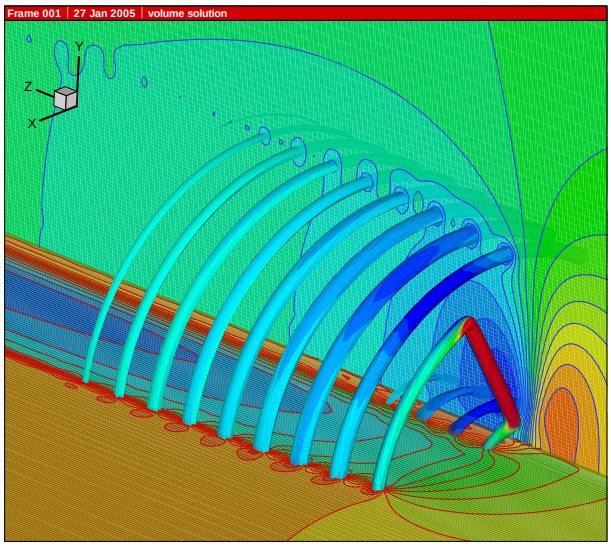

FIGURE 5.5. x=0-plane, pressure distribution; y=0-plane, streamwise velocity; iso surface, constant vorticity with a surface of a contour pressure distribution.

parameter, ϵ, see figure 5.6. Note that the radial position of the vortex core starts close to the tip. In section 3.3 the radial position of the vortex core was discussed. In this case, the vortex core does obviously originate close to the tip of the blade at a slightly lesser radial position than the blade tip.

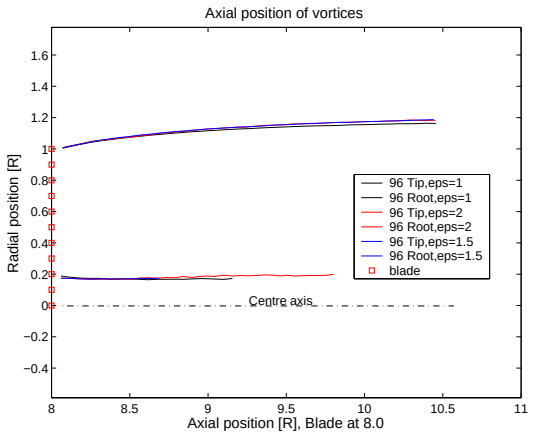

FIGURE 5.6. Position of vortex cores

5.2.5. *Phase difference between tip and root vortex*

Since the position of each vortex core is known, the phase difference between the tip and root spiral could be calculated. Figure 5.7 shows how the root vortex moves more slowly downstream compared to the tip vortex. The smearing parameter, ϵ, does affect the phase difference between tip and root vortices. Then this parameter affects the vortices to the extent that they actually moves with different velocities. This qualitative behaviour is to be expected from a theoretical standpoint using induction theory, where the tip vortex spirals decelerate the whole flow in the wake.

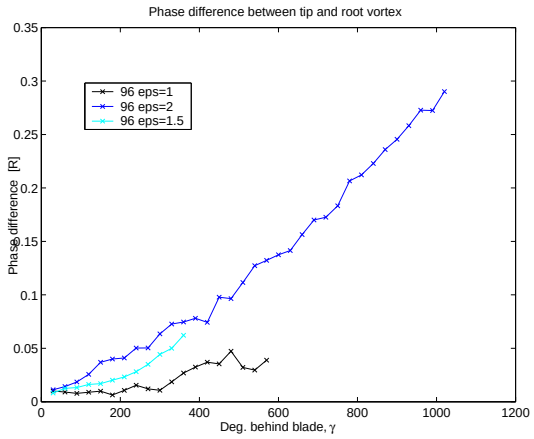

FIGURE 5.7. Phase difference between tip and root vortex core. The phase difference is defined as the difference in axial position between root and tip vortex, at the same rotational angle behind the blade, i.e. the ACL. A smaller value of ϵ represents a tighter volume force

5.2.6. *Reynolds numbers dependence*

Simulations with six different Reynolds number were performed, see figure 5.2. Figure 5.8 and 5.9 show iso surfaces of the vorticity. Figure 5.9 has a higher value of Reynolds number. One can see that for the case with higher Reynolds number, the vortex spiral can be traced further downstream, as expected, since the viscosity, in the Re3 case, to a greater extent destroys the structure of the wake.

When investigating the dependence of the Reynolds number, the value of the power coefficient, C_p (defined in equation (2.4)), was used in the analysis, see figure 5.10.

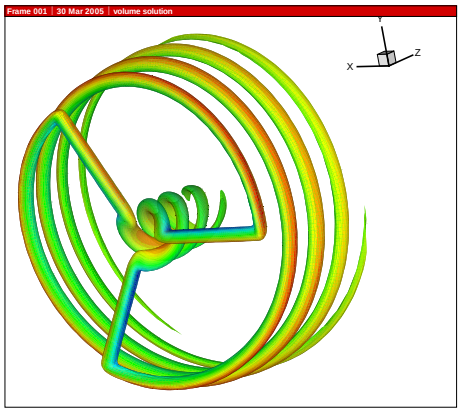

FIGURE 5.8. Iso surface of constant vorticity, $\zeta = 4.95$, with contour of streamwise velocity distribution. $Re = 3{\cdot}10^5$ (Re3).

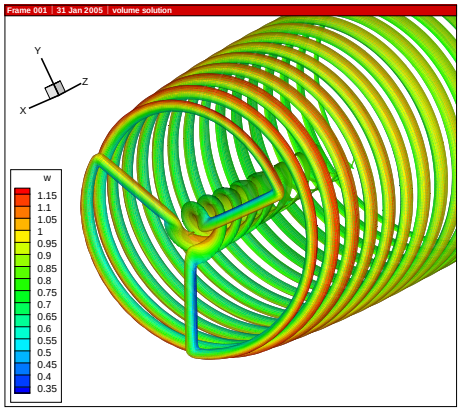

FIGURE 5.9. Iso surface of constant vorticity, $\zeta = 4.95$, with contour of streamwise velocity distribution. $Re = 3{\cdot}10^6$ (Re4).

Mikkelsen did the same type of analysis for the actuator disc method, [Mikkelsen]. He shows that when reaching high enough Reynolds number, the value of C_p converges toward a stationary value. The same behaviour can be seen when using the ACL method. Therefore, the conclusion can be made, that when using high enough Reynolds number, the Reynolds number does not affect the power coefficient.

Figure 5.10 indicates that the change in the C_p value, for high Reynolds number, decreases with increasing number of mesh points. Therefore, one can conclude that the difference between the C_p curves, at high Reynolds number,

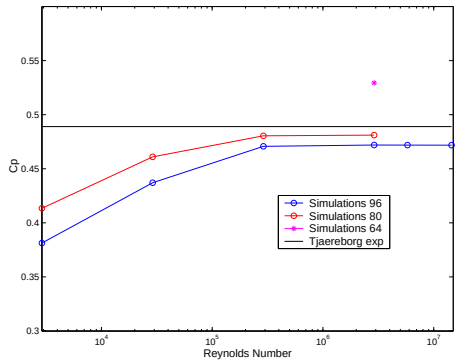

FIGURE 5.10. Cp values dependency on grid size and Reynolds number, i.e. viscosity. The viscosity for air is $16,7 \cdot 10^{-6} Nsm^{-2}$ which in this case corresponds to a Reynolds number of $\approx 1.8 \cdot 10^7$. The experimental Cp at 10 m/s is 0.489.

is because of numerical diffusion. When reaching a stationary level of the C_p value, i.e. independent of even larger grids, an Euler solution has been reached.

5.2.7. *Grid dependence*

In figure 5.10 one can see that the power coefficient depends on the grid size. The value of C_p converges with higher numbers of grid points, however, the converged value is about four percent lower than the experimental based value. Mikkelsen, [Mikkelsen], showed that when using the ACD method, the deviation from experimental values was in the same order but in the ACD case, the power was overestimated instead as when using the ACL method, when the power is underestimated.

However, power is extremely difficult to measure in reality frequently depending on the accuracy of the anemometer used. The difference between calculation in terms of C_p is, therefore, not necessarily indicative of calculation inaccuracy.

5.3. Evaluation method

Since one of the main aims with this project is to find and evaluate a method which will make it possible to understand more about the flow in the wake and especially circulation, see section 3.2. It is quite possible to study different aspects of how this method can result in better understanding of the wake and its circulation. This section will therefore deal with a method developed within this project to evaluate the circulation. A knowledge of the positioning of the vortices and their strength of circulation can be used as a base for engineering methods utilizing induction theory for loads and performance prediction.

The performed simulations have given the entire flow field. When the circulation is evaluated in the wake, an integration is performed around a loop, enclosing the vortex. Each vortex is evaluated in terms of its circulation in a plane perpendicular to the turbine disc, see figure 5.11.

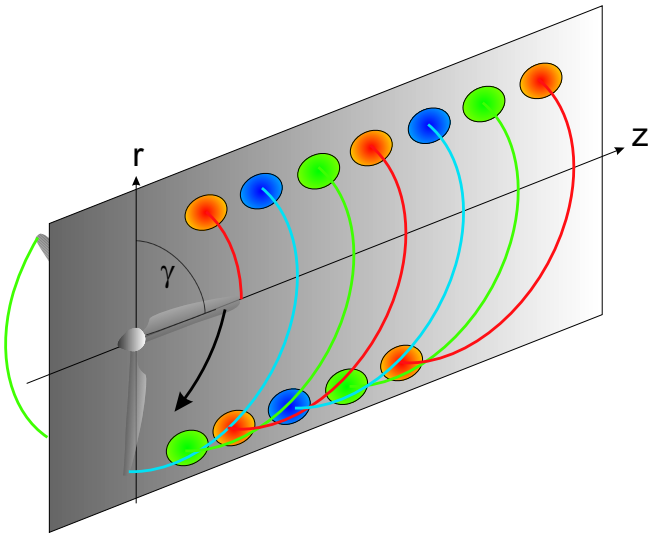

FIGURE 5.11. The vortices are evaluated in planes orthogonal to the turbine plane. Every third vortex originates from the same blade. The angle between the blade, i.e. the actuator line, and the location of the evaluated vortex in rotational sense is defined as γ.

Figure 5.12 shows how the circulation is evaluated. The vortex created at the tip, or at least close to the tip, is evaluated every 30° behind the blade. The root vortex is evaluated in the same manner. As can be seen in figure 5.12 the vortices tend to be smeared out further downstream because of diffusion. Therefore, it is more difficult to evaluate the circulation further downstream.

The circulation is integrated at a specific value of the vorticity. In that way, one makes sure that the integration is done in a coherent manner and can be compared at different positions.

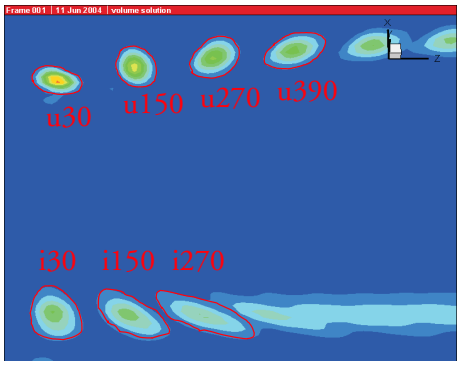

FIGURE 5.12. An integration is performed around each vortex to get the circulation. u indicates the tip vortex, i the root vortex, 30 150 etc represents degrees of azimuth behind the actuator line. The red line represents the integration path.

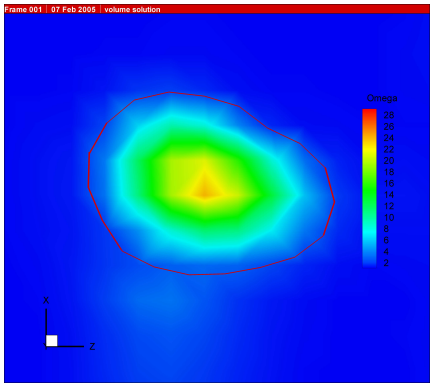

FIGURE 5.13. An integration is performed around each vortex to get the circulation, see equation 3.2 The red line represents the integration path.

Figure 5.13 shows an area with a vorticity level that differs from the mean value in the flow field, which is surrounded by an integration path. By choosing the integration path in this way, one makes sure that the entire vortex is surrounded by it.

Figure 5.14 shows the mesh with 96 points at each block side. One can see that the resolution, however, could be better. When evaluating the circulation sensitivity to different parameters, the mesh size might affect the results. The integration is performed by choosing a number of evaluation points at the integration path. The values at these points are then reached by an interpolation (2nd order) between surrounding grid points. A mesh with too few grid point might therefore give numerical errors. The number of grid points does, however, affect the computational time to a great extent.

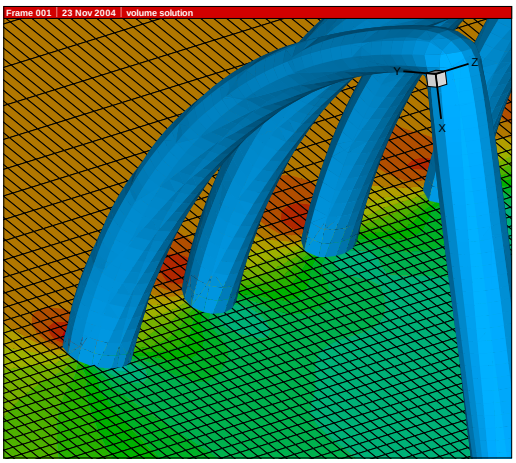

FIGURE 5.14. Closeup of the mesh in the integration area.

5.4. Evaluation of the circulation

This section shows results from the simulations with the evaluation method described i the previous section.

5.4.1. *Epsilon dependence*

The sensitivity of the circulation with the respect to ϵ has been evaluated. The evaluation was performed with three different grid sizes, 64, 80 and 96 node points at each side of the blocks as discussed in section 5.1. The results can be seen in figure 5.15.

The solution converges when ϵ approaches one. The wiggles that appear some distance downstream in figure 5.15 can probably be explained by too few number of grid points when the circulation is integrated, see figure 5.14, and because of increasing smearing of the cores further downstream. The computation time does however increase rapidly with increasing number of grid points.

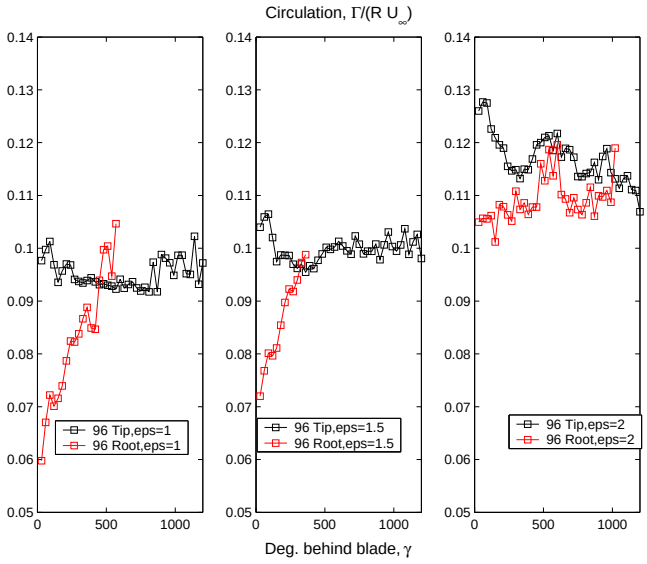

FIGURE 5.15. The figure shows simulations with the largest mesh, i.e. 96 points at each block side, with different values on ϵ. A small value of ϵ represents a tighter volume force distribution around the blade.

5.4.2. *Grid dependence*

The sensitivity of the circulation with respect to the grid resolution has also been evaluated. The evaluation was performed with three different grid sizes, 64, 80 and 96 node points at each side of the blocks as discussed in section 5.1. The results can be seen in figure 5.16.

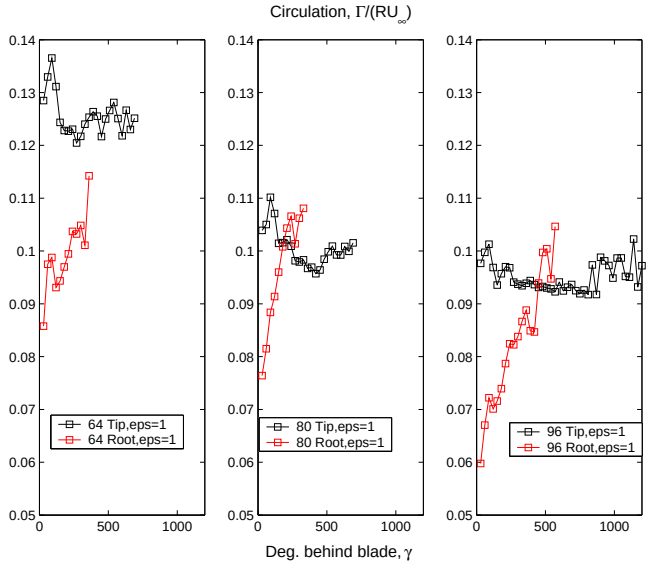

FIGURE 5.16. Simulation for the Tjaereborg turbine. Meshes with 64, 80 and 96 node point on each block side have been performed

The solution converges with greater grid size. The wiggles that appear some distance downstream in figure 5.15 and 5.16 can probably be explained by the same reason as when evaluation the dependence on ϵ. When using a finer grid, the integration could be performed further downstream without large fluctuations in the result. This is because the vortices are more concentrated further downstream with a finer mesh, and therefore it is also possible to perform the integration further downstream.

5.4.3. *Reynolds number dependence*

As mentioned in section 3.2 the circulation at the tip and root should, at least for inviscid flows, correspond to the maximum bound circulation at the blade. The circulation at the blades is given in figure 5.17. The circulation distribution represents the lift force; therefore, the lift force curve would have a similar curvature. The maximum normalized circulation at the blade is 0.10.

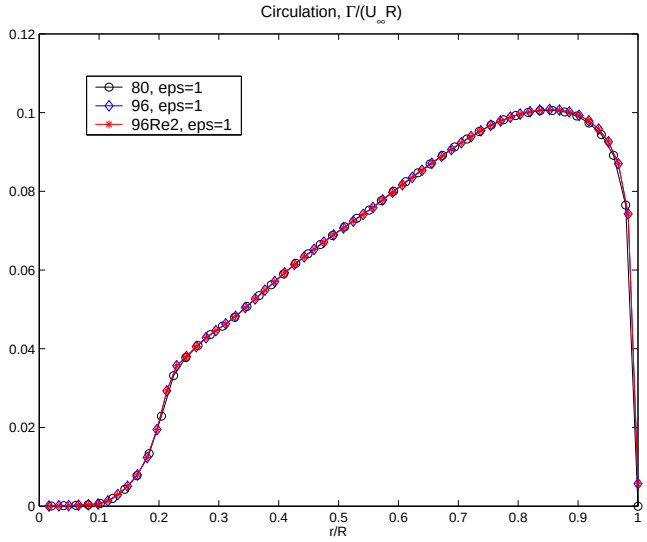

FIGURE 5.17. The figure shows the circulation distribution along the blade calculated with a mesh of 80 and 96 node points on each block side. Two different Reynolds number have been used with the 96 point mesh.

A comparison between the results of the 96 point mesh and $\epsilon = 1$ with the maximum circulation at the blade can be seen in figure 5.18.

The wiggles starting about 500 degrees behind the blades for the root vortex and about 800 degrees behind the blade for the tip vortex do most likely depend on integration errors when integrating the circulation. At these positions the vortex core starts to be smeared out and it is therefore also becoming difficult to identify a good integration path.

The result does however correspond fairly well with classical theories from Helmholtz. The tip vortex leaves the blade with a circulation value close to the maximum bound circulation at the blades. The root vortex does, however, leave the blade with a much lower value of the circulation. The circulation in the root vortex does, however, increase rapidly and reaches values at the same order as the bound circulation. The reason why the root vortex is smeared out earlier than the tip vortex is partly because the vortex cores are located closer together at the root and partly because of the radial gradient of the circulation.

The reason why the root vortex circulation grows faster with increasing Reynolds number does however still need to be answered.

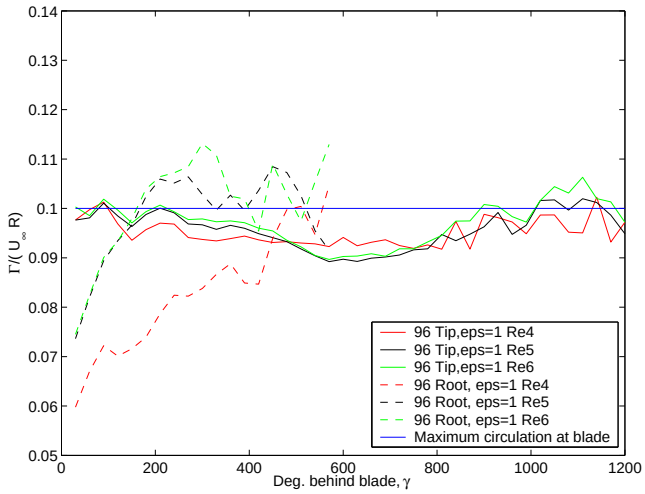

FIGURE 5.18. The figure shows the circulation distribution in the wake compared with the maximum circulation at the blade.

5.5. Evaluation of the vortex core

The vorticity and velocity in the vortex core were evaluated. Points along a line in the radial direction were extracted, see figure 5.19. The choice of direction of that line will affect the distributions since the vortices are not circular since they are stretched in the streamvice direction. The velocity will also differ at the same radius of the vortex.

Figure 5.20 shows the vorticity and velocity distribution in the vortex core 30° behind the actuator line in rotational sense, i.e. $\gamma = 30°$ according to figure 5.11, with different Reynolds number. The vorticity in the centre increases with increasing Reynolds number. One can also note that the radius of the vortex core decreases with increasing Reynolds number. The velocity distribution could be compared with figure 3.1. Negative values of vortex position correspond to the core half closest to the centre line and vice versa. That is obvious that the velocity distribution has a jump in velocity, compare with figure 3.1. It is because this vortex is positioned in a velocity field that is not constant since the outer part, positive vortex position, experiences a higher velocity than the inner part, with negative vortex position. From velocity profiles, one can say that the rigid body rotation area decreases while the gradient increases in the rigid body area with increasing Reynolds number. These figures are, however, to a great extent dependent on the grid size. In theory, the area below the vorticity functions would be constant, i.e. a flow with low Reynolds number means that the vortex is larger with a less intensive core. While a flow with higher Reynolds number experiences vortices which are smaller but much more

intensive in the vortex core. Therefore, the Reynolds number does not affect the vortex strength but the radial distribution. A low Reynolds number increases the diffusion of the vortex, therefore a low Reynolds number results in a shorter lifetime of the distinct wake spiral.

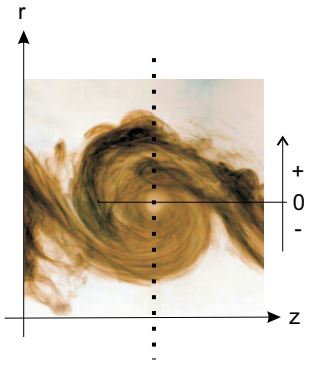

FIGURE 5.19. Definition of evaluation points in vortex area.

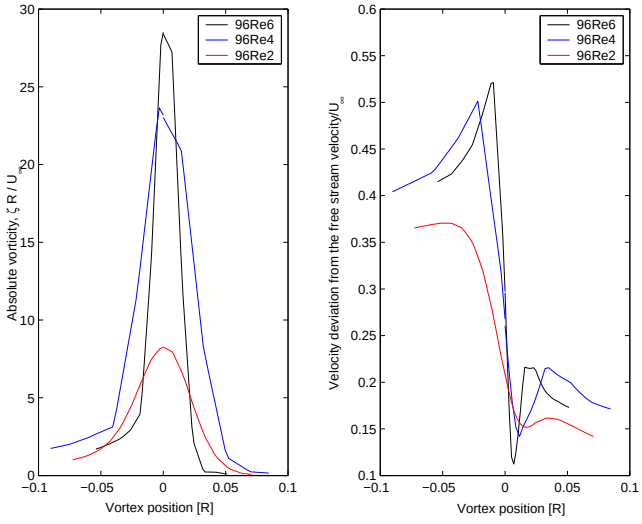

FIGURE 5.20. The figure shows the vorticity and velocity distribution in the vortex core 30° behind the actuator line in rotational sense at different Reynolds number with the 96 point mesh.

Figure 5.21 shows the vorticity and velocity distribution of the vortex core positioned at different positions in the field when Reynolds number is Re6. The vorticity and velocity distributions are plotted for core positions of γ equal to 30, 150, 270 degrees etc, where the angle γ is defined according to figure 5.11.

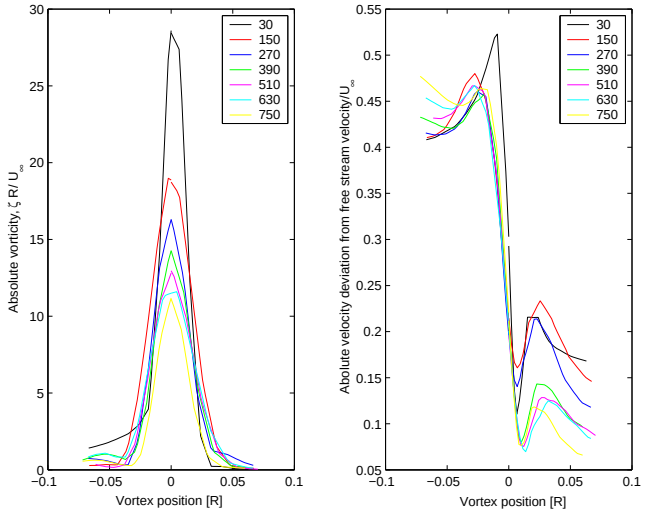

FIGURE 5.21. The figure shows the velocity deviation from the free stream velocity for a computation with Re6. The velocity distributions been extracted from an vertical line through each vortex core. The figure shows the velocity distribution at different positions behind the actuator line. Each position is noted by the angle γ in rotational sense, see figure 5.11.

In figure 5.21 one can see that the vorticity decreases downstream in the wake, which is expected because of diffusion. It is also possible to see that the velocity for positive core positions decreases downstream while the velocity for negative core positions, i.e. closest to the centre line, seams to change less. The outer part of the vortex cores tends to adapt the velocity toward the free stream velocity.

The vorticity in the core centre was extracted from the flow field. The results for cases with a Reynolds number of Re4 are shown in figure 5.22. The figure shows that the vorticity increases with decreasing value of ϵ. One can also note that the vorticity is dependent of the grid size. The level of the vorticity in the core could therefore be said to in a great extent be dependent of the smearing parameter and the mesh size.

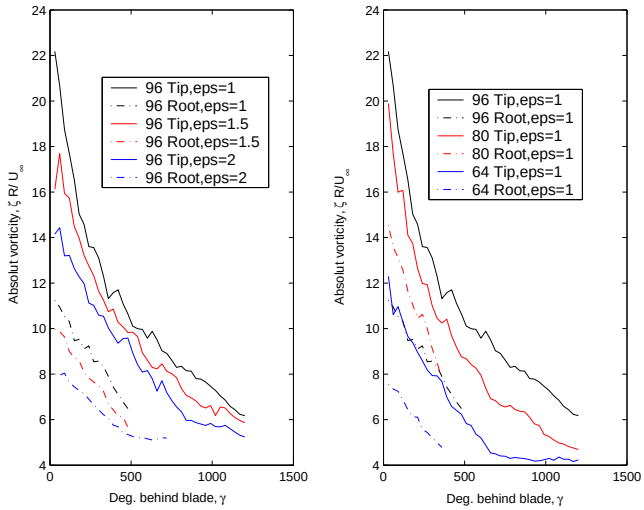

FIGURE 5.22. Vorticity in the vortex core. Left: Vortex dependency of smearing function. Right: Vortex dependence of grid size.

CHAPTER 6

Conclusions

6.1. Conclusions

Fulfillment of the aims

The aim of this project was partly to evaluate existing simulation methods to be able to choose a method appropriate for the main aim, that is to get a better understanding of the flow behavior in the wake. The results from the actuator line method were very successful. Mainly because it gave results which made it possible to track the tip and root vortex and therefore made it possible to evaluate essential features in the wake. The method also made it possible to run these simulations in reasonable computational times.

The method has been proved to give reasonable results compared with measurements when considering power. An evaluation of the sensitivity of the Reynolds number resulted in a greater understanding of the numerical method. Some questions still remain considering the effect of different Reynolds numbers when simulating the circulation.

An evaluation of numerical parameters such as ϵ and grid size resulted in a greater understanding of sensitivities in the numerical method.

From the evaluation of the flow field in the vortex and its core it is possible to conclude that the simulation resulted in a flow field that corresponds well to expected vortex behaviour.

All this together gives a good foundation for future work in this area, since the project resulted in:

- Knowledge of a suitable numerical method.
- Access to software and computer resources needed to perform simulations. (Cooperation with DTU)
- Evaluation methods and code to extract circulation data in the wake.
- Some basic understanding of the wake structure.

Remaining questions

The results show that with a mesh of 96 node points on each block side and an ϵ at a value of 1, gives a converging solution that corresponds fairly well to what is expected from Helmholtz' classical theorem. The result did however show a slow decrease of the circulation downstream while neglecting the uncertain part with wiggles, which starts about $\gamma = 800$ for the tip vortex. The question arises, if the value of the circulation in the wake is less than the maximum circulation at the blade only because of numerical errors or from viscous effects? As discussed earlier, the circulation in the wake should correspond to the maximum circulation on the blades at least in inviscid theory.

As mentioned above, the increasing growth of circulation with increasing Reynolds number is an unanswered question. More effort is therefore needed to understand this problem.

The knowledge about the numerical behaviour, such as dependence of ϵ, has increased during the project. The position and strength on the vortex cores depends on the ϵ parameter, therefore it is necessary to verify and calibrate this method by comparing it with results from full scale measurements.

This project gives, as mentioned, a good base for future work, where many questions remains to be resolved.

Further work

Future work will be focused on verification of these results. However, today it is not possible to compare with measurements since there are no experimental wake data of good enough quality available.

Hopefully, the NREL project MEXICO could provide necessary experimental data, which will make it possible to compare these simulations with measurement results of a at least model scale experimental set up. The MEXICO project was originally scheduled to be finalized in 2003 but has been delayed until 2005.

Future work, based on both numerical and experimental methods, will aim at a better understanding of the physics of the wake. With increasing confidence in the methodology developed during this effort, the numerical "wind tunnel" is seam to emerge. It is tentatively concluded that future data from continued development of this method will be very useful in the development of engineering methods for loads and performance prediction. Such engineering methods depend on vortices and induction theory where the Biot Savart's law is utilized. The CFD method presented here provides the vortex pattern necessary for such development work.

Bibliography

Alfredsson, P-H., Dahlberg, J-Å., *A preliminary wind tunnel study of windmill wake dispersion in various flow conditions*, Technical Note AU-1499, Part 7, FFA, Stockholm, Sweden, September 1979.

Andersson, M. B., *A Vortex-wake Analysis of a Horizontal Axis Wind Turbine and a Comparison with Modified Blade Element theory*, Proceedings of the Third International Symposium on Wind Energy Systems, Copenhagen, BHRA Fluid Engineering, paper no. H1,pp, 357-74, 1980.

Betz, A., *Das maximum der theoretisch möglichen ausnützung des windes durch windmotoren, Zeitschrift das gesamte Turbinewessen*, pp 307-309, 1920.

Burton, T., Shape, D., Jenkins, N., Bossanyi, E., *Wind Energy Handbook*, John Wiley and Sons, Ltd, West Sussex, 2001.

Carlén, I., *Structural analysis of wind turbine blades - 3D modelling and slender element approximations*, Teknikgruppen AB, TG-R-05-03, 2005a.

Carlén, I., *SOLDE - A tool for finite element deflection analysis of wings*, Teknikgruppen AB, TG-R-05-04, 2005b.

Dahlberg, J-Å., *In private communication he showed unreported test results from a small turbine (20cm diameter) where aerodynamic blades extended from about 25-30 % radius with minimal support structure. This emanated a turbine with no nacelle or hub*, FOI, 2005.

Efraimsson, G., Petrini, E., Nordström, J. *Errors in Numerical Simulations of Vortices*, Submitted to Computers and Fluids, 2005.

Eggeston, D. M., Stoddard, F. S., *Wind turbine Engineering design*, Van Nostrand Rheinhold, New York, 1987.

Freris, L. L., *Wind Energy Conversion Systems*, Cambridge University Press, Great Britain, 1990.

Ganander, H., *Method for Stability Analysis based on the Floquet Theory and Vidyn Calculations*, Teknikgruppen AB, 2005.

Gluert H., *Aerodynamic Theory*, Volume 4, Julius Springer, Division L, pp.169-360, Berlin, Germany, 1935.

Gluert, H., *The elements of airfoil and airscrew theory*, Cambridge University press, Cambridge, England, 1926.

Helmholtz, H. L. F., *Über Integrale der Hydrodynamischen Gleichungen, welche den Wirbelbewegungen ensprechen.*

Lanchester, F. W., *A contribution to the theory of propulsion and the screw propeller.*, Transaction of the Institution of Naval Architects, 1915.

Manwell, J. F., McGowan, J. K., Rogers, A. L., *Wind Energy Explained, theory, design and application*, John Wiley and Sons Ltd, West Sussex, England, 2002.

Mast, E. H. M., *Estimating the circulation distribution using near wake velocity measurements*, Delft University of Technology, 2003.

Menter, F. R., *Zonal Two Equation $k-\omega$ Turbulence Models for Aerodynamic Flows*, AIAA-paper-932906, 1993.

Michelsen, J. A., *Basis3D - a platform for development of multiblock PDE solvers*, Report AFM 92-06, Dept. of Fluid Mechanics, Technical University of Denmark, DTU, 1992.

Michelsen, J. A., *Block structured multigrid solution of 2D and 3D elliptic PDE's*, Report AFM 94-06, Dept. of Fluid Mechanics, Technical University of Denmark, DTU, 1994.

Mikkelsen, R., *Actuator Disc Methods Applied to Wind Turbines*, MEK-FM-PHD 2003-02, 2003.

Montgomerie, B., *Vortex Model for Wind Turbine Loads and Performance Evaluation*, Swedish Defence Research agency, FOI-R–1301–SE, 2004a.

Montgomerie, B., *Methods for Root Effects, Tip Effects and Extending the Angle of Attack Range to $\pm 180^{\circ}$, with Application to Aerodynamics for Blades on Wind Turbines and Propellers*, Swedish Defence Research agency, FOI-R-1305–SE, 2004b.

Montgomerie, B., Dahlberg, J-Å., *Vortex Systems studies on small wind turbines*, Swedish Defence Research agency, FOI-R–0936–SE, 2003.

Snel, H., Houwink, R., Piers, W. J., *Sectional prediction of 3D effects for seperated flow on rotating blades.*, Proceedings of the ECWEC '93 Conference, p395-9, 1993.

Spalart, P. R., Allmaras, S. R., *One-equation Turbulence Model for Aerodynamic Flows*, La Recherche Arospatiale, 1:5-21, 1994.

Spalart, P. R., Jou, W-H., Strelets, M., Allmaras, S. R., *Comment on the Feasibility of LES for Wings, and on Hybrid RANS/LES approach*, Proceeding of 1st AFOSR Int. Conf. on DNS/LES, Ruston, LA, August 4-8. Greyden Press, Columbus, OH, 1997.

Sørensen, J. N., Kock, C. W., *A Model for unsteady rotor aerdynamics*, Journal of Wind Energy and Industry Aerodynamics, 58:259-275, 1995.

Sørensen, J. N., Shen, W. Z., Munduate. X., *Analysis of wake states by a full-field actuator disc model*, Wind Energy, 1:73-88, 1998.

Sørensen, J. N., Myken A., *Unsteady actuator disc model for horizontal axis wind turbine*, Journal of Wind Engineering and Industry Aerodynamics, vol. 39, 1992.

Sørensen, J. N., Shen, W. Z., *Numerical Modeling of Wind Turbine Wakes*, Journal of Fluid Engineering, vol. 124, June 2002.

Sørensen, N. N., *General perpose flow solver applied to flow over hills*, PhD Dissertation, Risø National Laboratory, Roskilde, Denamark, 1995.

Sørensen, N. N., Johansen, J., *Application of a Detached-Eddy Simulation model on Airfoil Flows*, IEA, 2000.

Vermeer, L. J., Sørensen, J. N., Crespo, A., *Wind Turbine Wake Aerodynamics*, Progress in Aerospace science 39, p 486, 2003.

Wallin, S., Girimaji, S. S. *Evolution of an Isolated Turbulent Trailing Vortex*, AIAA Journal, No 38, p657-665.

Wilson, R. E., Lissaman, P. B. S., *Aerodynamic performance of wind turbines*, Energy research and development administration, ERDA/NSF/04014/1, 1976.

Wilson, R. E., *Aerodynamic behavior of wind turbines*, Wind turbine technology, Spera D. A., 1998.

Wizelius, T., *Vindkraft i teori och praktik*, Studentlitteratur, Lund, 2002

Åhlund, K., *Investigation of the NREL NASA/Ames Wind Turbine Aerodynamics Database*, Engineering degree thesis, Mälardalens Högskola, 2004.

Tjaereborg Data, *http://www.afm.dtu.dk/wind/tjar.html*.